UNIVERSITY OF CALIFORNIA
RIVERSIDE

Optothermal Raman Studies of Thermal Properties of Graphene Based Films

A Dissertation submitted in partial satisfaction
of the requirements for the degree of

Doctor of Philosophy

in

Electrical Engineering

by

Hoda Malekpour

March 2017

Dissertation Committee:

Dr. Alexander A. Balandin, Chairperson
Dr. Roger Lake
Dr. Alexander Khitun

The Dissertation of Hoda Malekpour is approved:

Committee Chairperson

University of California, Riverside

Acknowledgments

I would like to thank my PhD advisor Prof. Alexander Balandin for his encouragement, guidance and continuous support. As a PhD student working with Prof. Balandin I was provided by the opportunity to participate on novel and interesting research projects as well as collaborating with the most knowledgeable professors in my research area and I am grateful to Prof. Balandin for that. Moreover, he taught me a lot of writing and communication skills by encouraging me to attend different conferences and meetings. I am sincerely grateful for having the pleasure to work with such a knowledgeable and supporting advisor.

I am also thankful to Prof. Roger Lake and Prof. Alexander Khitun for serving as committee member in my dissertation. I am thankful to my collaborator Dr. Denis Nika who taught me a lot about physics and modeling of thermal transport. I am thankful to my other collaborator Dr. Konstantin Novoselov who is one of the most knowledgeable professors in graphene area. I would also like to thank my colleagues at nano device laboratory for providing a friendly and helpful research environment. And finally I would like to express my deepest gratitude to my parents Anoushirvan and Kobra and my sister, Farzaneh, for their patience, encouragement and endless support.

The text of this dissertation, in part or in full, is a reprint of materials appeared in the following journals:

- Nanoletters [1] reprinted with permission from American Chemical Society.

- Nanoscale [2] reprinted with permission from Royal Society of Chemistry.

The co-author A. A. Balandin, listed in the above publications directed and supervised the research which forms the basis for this dissertation. This work at UC Riverside was supported in part by the National Science Foundation (NSF) grant ECCS 1307671 on Engineering the Thermal Properties of Graphene, grant CMMI 1404967 on Engineering Defects in Designer Materials, UC Proof of Concept project on Graphene-Based Thermal Interface Materials and Heat Spreaders, DARPA Defense Micro-electronics Activity (DMEA) under agreement number H94003-10-2-1003, and STARnet Center for Function Accelerated nano-Material Engineering (FAME), Semiconductor Research Corporation (SRC) program sponsored by MARCO and DARPA.

Dedicated

To

My Parents

ABSTRACT OF THE DISSERTATION

Optothermal Raman Studies of Thermal Properties of Graphene Based Films

by

Hoda Malekpour

Doctor of Philosophy, Graduate Program in Electrical Engineering
University of California, Riverside, March 2017
Dr. Alexander A. Balandin, Chairperson

Efficient thermal management is becoming a critical issue for development of the next generation of electronics. As the size of electronic devices shrinks, the dissipated power density increases, demanding a better heat removal. The discovery of graphenes unique electrical and thermal properties stimulated interest of electronic industry to development of graphene based technologies. In this dissertation, I report the results of my investigation of thermal properties of graphene derivatives and their applications in thermal management. The dissertation consists of three parts. In the first part, I investigated thermal conductivity of graphene laminate films deposited on thermally insulating polyethylene terephthalate substrates. Graphene laminate is made of chemically derived graphene and few layer graphene flakes packed in overlapping structure. Two types of graphene laminate were studied: as deposited and compressed. The thermal conductivity of the laminate was found to be in the range from 40 W/mK to 90 W/mK at room temperature. It was established that the average size and the alignment of graphene flakes are parameters dominating the heat conduction. In the second part of this dissertation, I investigated thermal

conductivity of chemically reduced freestanding graphene oxide films. It was found that the in-plane thermal conductivity of graphene oxide can be increased significantly using chemical reduction and temperature treatment. Finally, I studied the effect of defects on thermal conductivity of suspended graphene. The knowledge of the thermal conductivity dependence on the concentration of defects can shed light on the strength of the phonon - point defect scattering in two-dimensional materials. The defects were introduced to graphene in a controllable way using the low-energy electron beam irradiation. It was determined that as the defect density increases the thermal conductivity decreases down to about 400 W/mK, and then reveal saturation type behavior. The thermal conductivity dependence on the defect density was analyzed using the Boltzmann transport equation and molecular dynamics simulations. The obtained results are important for understanding phonon transport in two-dimensional systems and for practical applications of graphene in thermal management.

Contents

List of Figures

List of Tables

Chapter 1

Introduction

1.1 Introduction to thermal connectivity

In physics, thermal conductivity is the property of a material to conduct heat. It is evaluated in terms of Fourier's law for heat conduction, based on which, the heat flux density ($\overrightarrow{q}$) is equal to the product of thermal conductivity (k) and the negative local temperature gradient (∇T):

$$\overrightarrow{q} = -K\nabla T \tag{1.1}$$

Thermal conductivity is measured in watt per kelvin per meter ($Wm^{-1}K^{-1}$). The reciprocal of thermal conductivity is called thermal resistivity. Another term, which is important to be defined, is thermal diffusivity. In heat transfer analysis, thermal diffusivity is the thermal conductivity divided by density and specific heat capacity at constant pressure. It has the

SI unit of $m2/s$:

$$\alpha = K\rho C_P \tag{1.2}$$

Where, K is thermal conductivity $(W/(mK))$, ρ is density (kg/m^3) and C_P is specific heat capacity $(J/(kgK))$. Thermal conductivity is a property that determines how much heat will flow in a material, while thermal diffusivity determines how rapidly heat will flow within it.

1.1.1 Thermal conductivity and heat conduction equation

Thermal conductivity of a material indicates its capability to conduct heat. It is defined as rate of heat flow divided by the cross section area and temperature gradient:

$$K = \frac{\Delta Q}{\Delta t}.\frac{1}{A}.\frac{1}{\nabla T} \tag{1.3}$$

Where $\Delta Q/\Delta t$ is rate of heat flow, A is the cross section area and ∇T is temperature gradient. The law of heat conduction, also known as Fourier's law, states that the rate of local heat flux, $\overrightarrow{q}$, is equal to the product of thermal conductivity, k, and the negative temperature gradient -∇T :

$$q = -K.\nabla T \tag{1.4}$$

By integrating this differential equation, the integral form of Fourier's law is obtained:

$$\frac{\delta Q}{\delta t} = -K \oint_s \nabla T.d\overrightarrow{A} \tag{1.5}$$

Where, $\delta Q/\delta t$ is the amount of heat transferred per unit time, dA is oriented surface area element. Integrating the above equation in a homogenous material of one dimensional

geometry between two endpoints at constant temperature gives heat flow rate as:

$$\frac{\Delta Q}{\Delta t} = -KA\frac{\Delta T}{\Delta x} \tag{1.6}$$

Where, ΔT is the temperature difference between the ends, Δx is the distance between the ends. This law forms the basis of derivation of heat conduction equation.

1.1.2 Limiting factors of thermal conductivity

Thermal conductivity of semiconductors is the sum of the lattice (phonon) k_{ph} and electronic k_e components. The characteristic ratio of these two obtained for doped semiconductors is $k_e/k_{ph} \sim 1/2$. For intrinsic silicon structures this ratio is even lower. Thus, for simplicity, we will only discuss the lattice (phonon) contribution to the thermal conductivity and neglect its electronic part [3] . Kinetic theory of gases gives the following expression for the lattice thermal conductivity:

$$K = \frac{1}{3}C_V.v.l \tag{1.7}$$

Where K is thermal conductivity, C_V is heat capacitance per unit volume, v is phonon group velocity and l is mean free path of particles between collisions. The phonon mean free path (MFP) is determined by three processes: boundary scattering, scattering by other phonons and impurity scattering. It is well known that the normal three-phonon scattering processes (N-processes) in which the total momentum is conserved cannot lead to a finite thermal resistance, although they influence it indirectly by redistributing phonon modes [4, 5]. Only processes, which do not conserve crystal momentum, contribute to the lattice thermal resistance. Such processes, referred as resistive, are boundary scattering, impurity scattering, and three-phonon Umklapp scattering process (U-process) in which the sum of

phonon wave vectors is not conserved but changes by a reciprocal-lattice vector.

At high temperature, all phonon modes are excited and substantial portion of phonon collisions will be U-process and the mean free path we be proportional to $1/T$. On the other hands, boundary scattering becomes important when MFP is comparable with the width of the sample. Based on Casimir limit the phonon-boundary scattering rate presented as:

$$\frac{1}{\tau_B} = \frac{v}{D} \tag{1.8}$$

Where, v is the group velocity of phonons and D is the lateral dimension. Impurity scattering, in its turn, can be separated for isotope scattering arising from the presence of atoms with different mass dislocation scattering, and scattering on atoms of different elements [3].

1.1.3 Different components of thermal conductivity

Heat can be conducted through a solid either by elastic waves in the crystal lattice or by free charge carriers. In metals it is generally sufficient to consider only the contribution to the flow of heat from the free electrons, hence the Wiedemann-Franz law relating electrical and thermal conductivities. On the other hand in semiconductors it is also necessary to take into account the contribution from the elastic waves, and the total thermal conductivity may be expressed as:

$$K = K_l + K_e \tag{1.9}$$

Where, k_l and k_e represents the lattice component and the electronic component, respectively. In most semiconductors, k_l is much greater than k_e but there are a few materials in which the magnitude of the two components may become comparable. It might be ex-

pected that k_e, should be related to the electrical conductivity by a relation similar to the Wiedemann-Franz law with a slightly different constant of proportionality due to the fact that degeneracy must be taken into account for metals, but not for semiconductors [6].

1.2 Methods of measuring thermal conductivity

1.2.1 Transient methods

In transient methods, measurement of thermal conductivity is performed during the process of heating up and the thermal gradient is recorded as a function of time. The advantage of these methods is that they can in general be performed more quickly, since there is no need to wait for a steady-state situation. An example of this method, which has been used in this dissertation, is Laser Flash Technique (LFT). The method is used to measure thermal diffusivity of different materials. An energy pulse heats one side of a plane-parallel sample. The temperature rise on the backside is detected as a function of time. The higher the thermal diffusivity of the sample, the faster the energy reaches the backside. Thermal diffusivity can be extracted from the measured temperature/time function on the backside of the sample.

A light source (xenon flash lamp) heats the sample from the bottom side and the temperature rise of the other side is measured as a function of time using an infrared (IR) detector. The measurement of the thermal diffusivity α and specific heat C_P allows the calculation of the thermal conductivity K, with an additional measurement or knowledge of the bulk density ρ of the sample material as shown in equation 1.10.

$$K(T) = \alpha(T) \times \rho(T) \times C_P(T) \tag{1.10}$$

Where, T is the temperature, K is the thermal conductivity, α is thermal diffusivity, ρ is the bulk density and C_P is the specific heat. Lase flash method can be used for measuring both the in-plane and cross-plane thermal conductivities, using different sample holders and masks. Fig. 1.1 shows an schematic of the masks and sample holders that is used for cross-plane and in-plane thermal conductivity measurements.

As shown in Fig. 1.1 (b), in-plane sample holder is designed so that the position of the energy input on the bottom side of the sample and the position of measuring the temperature increase on the top side of the sample (energy output) are located at different lateral positions. Thus the measured temperature increase of the sample shows the thermal diffusivity in a horizontal direction (in-plane).

1.2.2 Steady-state methods

In general, steady-state techniques perform a measurement when the temperature of the material does not change with time. This makes the signal analysis straightforward (steady-state implies constant signals). The disadvantage is that a well-engineered experimental setup is usually needed. Optothermal Raman (OTR) measurement is an example of this method that is widely used in this dissertation. In the next section, the OTR technique will be discussed in detail.

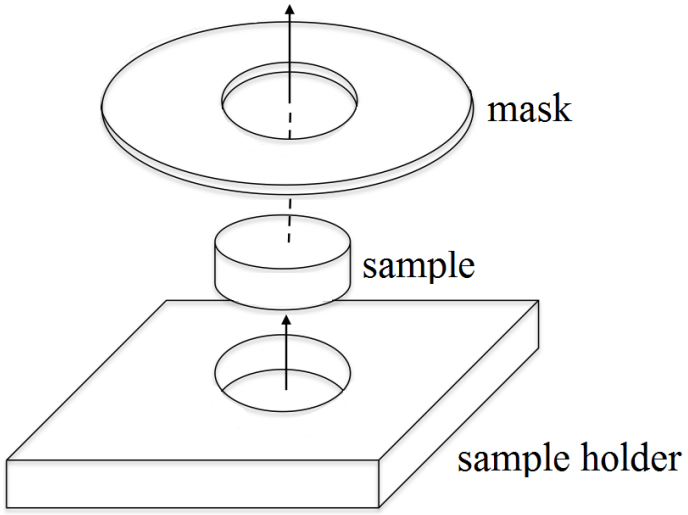

(a)

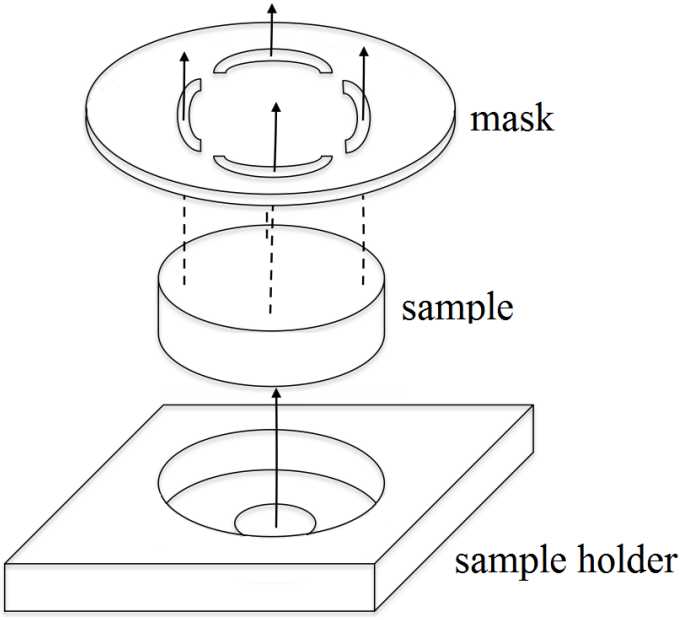

(b)

Figure 1.1: Schematic of thermal conductivity measurement, showing sample holders and masks for (a) cross-plane and (b) in-plane laser flash measurement. In both arrangements a flash lights heat the sample at one side and an IR detector reads the temperature rise at the opposite side of the sample. However, in-plane mask is designed so that the temperature reading occurs at different lateral position compared to the heating one. Therefore, the generated heat mostly travels in the in-plane direction to produce the corresponding temperature rise.

1.3 Optothermal Raman measurement of thermal conductivity

Optothermal Raman (OTR) is a direct steady-state measurement technique, which determines thermal conductivity directly without the need to calculate it from the thermal diffusivity data. In this technique, originally used for measuring the thermal properties of graphene [7], the micro-Raman spectrometer is used as thermometer to determine the local temperature rise. The temperature dependency of Raman peak position, give us the ability to read the temperature rise using Raman spectroscopy. This method is especially useful for graphene-based materials. Owing to graphenes distinctive Raman signature with clear G and 2D band, the temperature could be accurately read. The strong temperature dependency of Raman G band makes it perfect to be used as a mean of thermometry. That means the shift in the position of the graphene G peak can be utilized to measure the local temperature rise on the sample caused by laser heating. In this technique Raman excitation laser is also used as a heater. The measurement procedure involved two steps: the calibration measurements and the power-dependent Raman measurements. Both procedures will be discussed in the following sections.

1.3.1 Power-dependent Raman measurements

In the power-dependent Raman measurements, the position of Raman peak is read as a function of different laser power. In this measurement Raman excitation laser acts as a heater to cause local heating and thus peak shift. The power of laser is therefore chosen

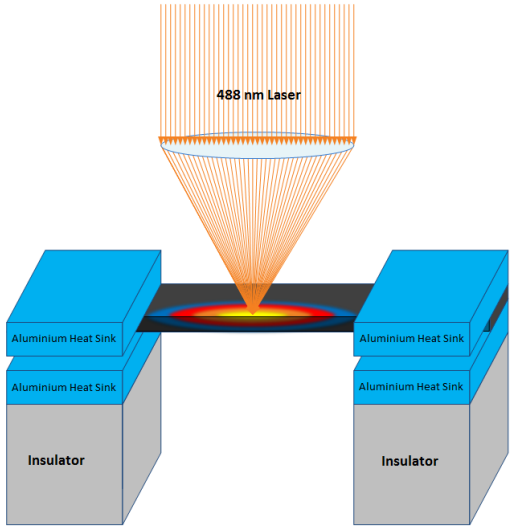

Figure 1.2: Schematic of the power-dependent Raman measurement with the specially designed sample holder.

to cause local heating. The shift in the peak is then recorded as a function of increasing power. In order to attribute this peak shift to temperature rise, calibration measurements need to be done.

For the power-dependent Raman measurements the sample is suspended over heat sinks. Therefore the Raman induced heat on the sample travels toward the heat sinks where the temperature remains at room temperature. Fig. 1.2 shows a schematic of this measurement. For this study we have designed a special sample holder to suspend macro size samples over two aluminum heat sinks. The power on the sample surface is then measured by replacing the sample with a power meter. The slope $\Delta\omega/\Delta P$ is then measured during this measurement were $\Delta\omega$ is the shift in Raman peak position and ΔP is the increase in excitation laser power. Knowing the sample geometry and temperature rise,

$\Delta T = \chi^{-1}\Delta\omega$, in response to the absorbed power, ΔP, one can determine the thermal conductivity K by solving the heat diffusion equation numerically. In order to determine χ, the temperature coefficient of Raman peak, calibration measurements need to be done. The details of calibration measurements and K extraction procedure are being discussed in the following sections.

1.3.2 Calibration measurements

The aim of calibration measurements is to attribute the Raman peak shift recorded during the power-dependent Raman measurements, to the laser induced temperature rise in the sample. The measurement is performed in the cold-hot cell (LINKAM THMS-600) with the temperature of the sample controlled externally (see Fig. 1.3). Low excitation power of the Raman laser is used to avoid any local laser induced heating. Since the low excitation power levels degrades the signal-to-noise (S/N) ratio, the exposure time should be increased achieve acceptable S/N ratio.

In the calibration measurements, the Raman peak position is recorded as a function of sample temperature, which is controlled externally using cold-hot cell. The slope of this plot determines the temperature coefficient of Raman peak (χ). It should be remembered that the χ value depends not only on the sample properties but also on the temperature range for which it was extracted. In the following section I will discuss how the thermal conductivity of sample is extracted having both calibration and power-dependent Raman measurements results.

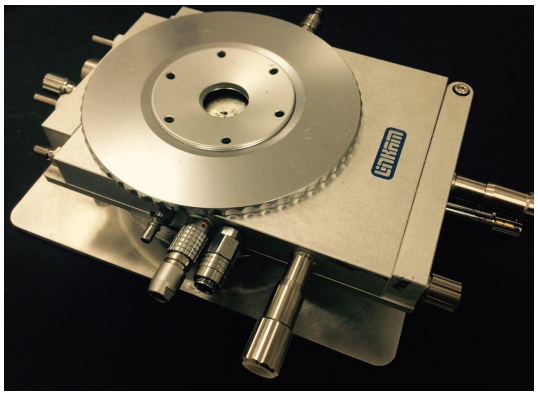

Figure 1.3: Optical image of the cold-hot cell, used to perform calibration measurements. The cell is designed to externally control the temperature of the sample with the accuracy of 0.1°C.

1.3.3 Thermal conductivity extraction

In order to extract the thermal conductivity Fouriers equation was solved for the specific sample geometry. Here I will discuss the heat diffusion equation for a 3D structure samples. COMSOL Multiphysics software package was used for numerical solution of the equation with proper boundary conditions. The laser spot heat source was assumed to have the Gaussian distribution of the power in the in-plane (x, y) direction. Considering penetration depth of the laser beam through the sample thickness (z), $P(x, y, z)$ can be written as:

$$P(x, y, z) = A \times exp(-\frac{x^2 + y^2}{2\sigma^2}) \times exp(-\frac{z}{d}) \tag{1.11}$$

Where, A is the amplitude defined from the total laser power, P_{tot}, σ is the standard deviation of the Gaussian distribution function defined from the laser spot size and d is the laser penetration depth. A is defined so that the integral of $P(x, y, z)$ over x, y, z is equal to the total applied power, therefore $A = P_{tot}/(2\pi d\sigma^2)$. σ is defined so that the full width at half maximum (FWHM) of Gaussian function is set to the laser spot size which itself is calculated having the numerical aperture of the objective lens and the laser wavelength

$(2\lambda/(\pi NA))$. Finally penetration depth, d is defined based on the refractive index of the material and the laser wavelength [8].

Considering our special designed sample holder (Fig. 1.2), the two ends of the suspended sample are attached to the heat sinks, which are modeled as being at RT. All other boundaries are defined as insulated from the environment, which means that the temperature gradient across the boundary is set to zero:

$$\overrightarrow{n}(K\nabla T) = 0 \tag{1.12}$$

The heat diffusion equation is solved via the iteration procedure. The total power and the thermal conductivity are entered as the inputs to the equation and the temperature distribution is determined as the result of simulations. The simulated temperature rise is compared with the measured temperature in the laser spot. The thermal conductivity is adjusted to higher or lower value based on the comparison. The task is simplified by introducing the slope parameter:

$$\theta = \frac{\partial \omega}{\partial P} = \chi \frac{\partial T}{\partial P} \tag{1.13}$$

The simulated plot of K vs. θ gives the actual value of thermal conductivity K for the measured value of the slope θ.

1.4 Outline of the dissertation

This dissertation consists of three parts:

1. Thermal conductivities of graphene laminate films deposited on polyethylene terephthalate substrates were studied. Two types of graphene laminate were investigated, as

deposited and compressed, in order to determine the physical parameters affecting the heat conduction the most. The measurements were performed using the optothermal Raman technique and a set of suspended samples with the graphene laminate thickness ranging from 9 μm to 44 μm. The thermal conductivity of graphene laminate was found to be in the range from 40 W/mK to 90 W/mK at room temperature.

2. Thermal conductivity of chemically reduced freestanding graphene oxide film annealed at 300 $^{\circ}C$ was studied. Both the in-plane and cross-plane thermal conductivities were measured using a combination of two different techniques: Raman opto-thermal and laser flash. The in-plane thermal conductivity values of 11-45 W/mK have been achieved in the reduced graphene oxide films, which show up to 15 times increased thermal conductivity comparing to reported values of free-standing GO film.

3. Thermal conductivity of suspended graphene was studied as a function of the density of defects, N_D, introduced in a controllable way. Graphene layers were synthesized using chemical vapor deposition technique and transferred on transmission electron microscopy greed, suspended over its ~ 7.5 mm size square holes. The defects in graphene lattice were induced by the low-energy electron beams (20 kV) and quantified by their Raman spectrum using D to G peak intensity ratios. It was found that as the density of defects changes from $\sim 2.0 \times 10^{10}$ cm^{-2} to $\sim 1.8 \times 10^{11}$ cm^{-2} the thermal conductivity, K, reduces from $\sim (1.8 \pm 0.2) \times 10^{3}$ W/mK to $\sim (4.0 \pm 0.2) \times 10^{2}$ W/mK at room temperature. At higher N_D, the thermal conductivity reveals an intriguing saturation behavior. The behavior was analyzed within the Boltzmann transport equation approach and molecular dynamics calculations.

Chapter 2

Graphene laminate as a conductive coating for plastic

Due [1] to the large use of plastic in electronic packaging, there is a strong practical motivation in thermally conductive coatings for various plastic materials. While being robust, lightweight and easy-to-work with materials, plastics suffer from very low values of thermal conductivity. Graphene laminate (GL) is a type of graphene-based material that can be conveniently utilized in coating applications [9]. Graphene and few layer graphene (FLG) flakes in GL layers, which are chemically derived, are closely packed in overlapping structure. It is common to deposit (spray on) GL films on polyethylene terephthalate (PET) substrates. Due to PETs extremely low thermal conductivity, ranging from 0.15 W/mK to 0.24 W/mK at room temperature, its applications have certain limits.

[1] This section of dissertation follows the published material from H. Malekpour, K. H. Chang, J. C. Chen, C. Y. Lu, D. L. Nika, K. S. Novoselov, A. A. Balandin, *Nano Lett.* **14**, 5155 (2014)

Coating PET with graphene laminate can lead to new applications domains. Graphene laminate consists of overlapping graphene and FLG flakes. Due to the random nature of graphene flakes overlapping regions, a large distribution of the flake sizes and thicknesses as well as presence of defects and disorder, the physics of heat conduction in such materials is non-trivial. Having the knowledge of thermal properties of GL layers and understanding materials parameters that limit heat propagation facilitates optimizing GL thermal coatings for practical applications. Here I investigated the thermal conductivity of GL-on-PET on a set of as deposited and compressed samples with different mass densities and GL thickness ranging from $\sim 9\ \mu m$ to $\sim 44\ \mu m$. In the following, I will review the sample structure followed by the outline of thermal measurements and experimental results. At the end of the section, I will outline the theory of heat conduction in FLG used to assist in the theoretical data analysis.

2.1 Preparation of graphene laminate on PET substrates

The samples for this study [1] were provided by University of Manchester and Bluestone Global Tech. GL layers were derived chemically and deposited on PET substrates. For this purpose, an aqueous dispersion of graphene nano-flakes was used as the coating ink. The dispersion of graphene flakes is assisted by the presence of the surfactants for deposition of a homogenous film. A conventional PET film was used as a substrate. The PET is a plastic material widely used in various containers. First, the substrate is coated by graphene ink using a laboratory slit coater. The coated substrate is then dried at low temperature to form GL-on-PET samples. Some of the samples were roll compressed and thus the samples

Table 2.1: Sample nomenclature, physical and thermal characteristics

GL-on-PET	Laminate Thickness $[\mu m]$	Average Flane Size $[\mu m]$	$K[W/mK]$	Note
1	44	1.10	40.0 ± 7.5	Uncompressed
2	14	1.15	59.0 ± 3.6	Uncompressed
3	13	1.24	75.5 ± 11.3	Uncompressed
4	9	1.18	90.0 ± 9.4	Compressed
5	24	1.07	63.5 ± 4.0	Compressed
6	30	0.96	44.5 ± 6.9	Compressed

were denoted uncompressed and compressed. The samples were then analyzed to better understand the characteristics of the laminate. Fig. 2.1 shows top view SEM micrographs of both uncompressed and compressed GL-on-PET. One should notice that the laminate is made of overlapping single layer graphene and FLG flakes with different size and shape. The cross-sectional SEM of the GL-on-PET is also shown in Fig. 2.2 with distinguished GL layer. The cross-sectional SEM is used to determine the thickness of laminate ranging from $\sim 9\ \mu m$ to $\sim 44\ \mu m$. An average value among several locations was used for this analysis due to the thickness non-uniformity. Moreover, the sheet resistance of the graphene laminate was measured by the 4-point probe technique and found to be within the 1.8 Ω/□ - 6.1 Ω/□ interval. The mass density of GL layers was found to vary from 1.0 g/cm^3 to 1.9 g/cm^3. Table 2.1 summarizes some of the GL properties used for this study.

2.2 Statistical analysis on the average flake size

For further quantitative analysis of thermal properties, an accurate statistical analysis has been done on the laminate flake size. As confirmed by SEM (Fig. 2.1), the GL is made

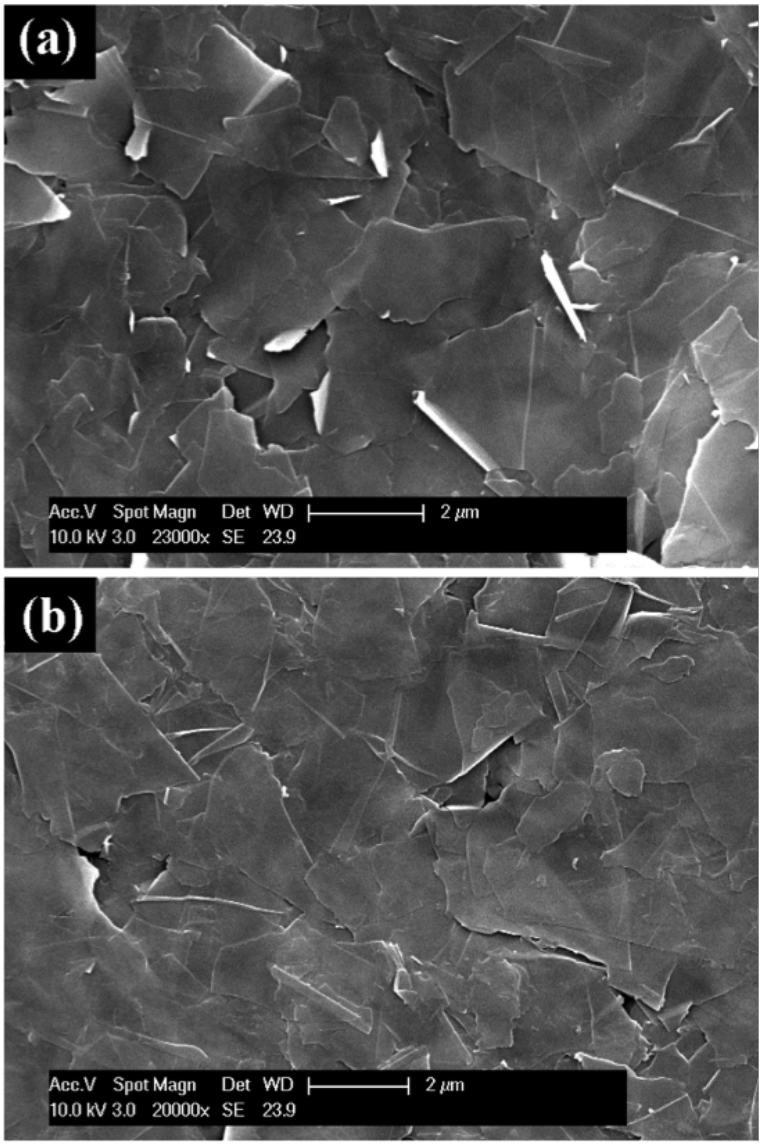

Figure 2.1: Top-view SEM images of the (a) uncompressed (sample 3) and (b) compressed (sample 4) GL-on-PET. Graphene laminate consists of the overlapping layers of graphene and FLG flakes with arbitrary shapes and random in-plane orientation. Although most of the flakes are aligned along the PET substrate some of the flakes reveal vertical orientation seen as bright white areas on SEM images. Note that the number of the misaligned vertical flakes is substantially reduced in the compressed GL-on-PET samples. The figure is reproduced from H. Malekpour, K. H. Chang, J. C. Chen, C. Y. Lu, D. L. Nika, K. S. Novoselov, A. A. Balandin, *Nano Lett.* **14**, 5155 (2014) with permission from American Chemical Society.

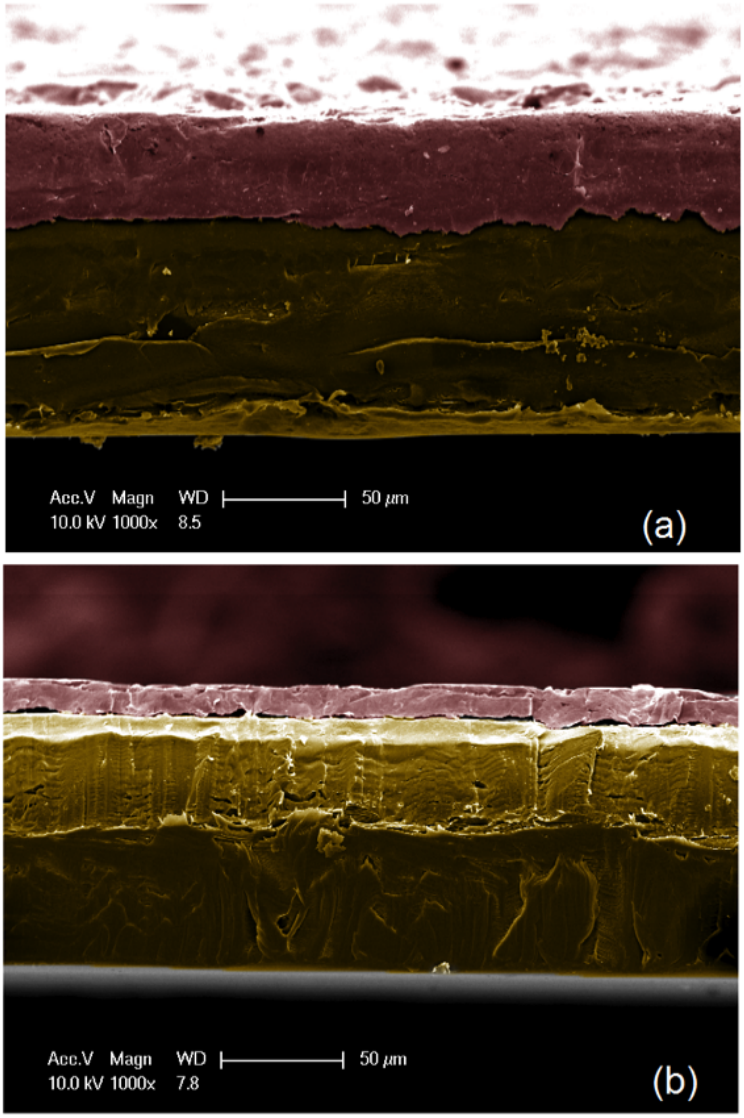

Figure 2.2: Cross-sectional SEM images of the (a) uncompressed (sample 2) and (b) compressed (sample 4) GL-on-PET. The pseudo colors are used to indicate the graphene laminate (burgundy) and PET (yellow) layers. The graphene laminate layer of the uncompressed sample is $\sim 44\mu m$ thick while the PET substrate is $\sim 110\mu m$ thick in the uncompressed GL-on-PET. The laminate thickness variation is clearly seen from the micrograph. The figure is reproduced from H. Malekpour, K. H. Chang, J. C. Chen, C. Y. Lu, D. L. Nika, K. S. Novoselov, A. A. Balandin, *Nano Lett.* **14**, 5155 (2014) with permission from American Chemical Society.

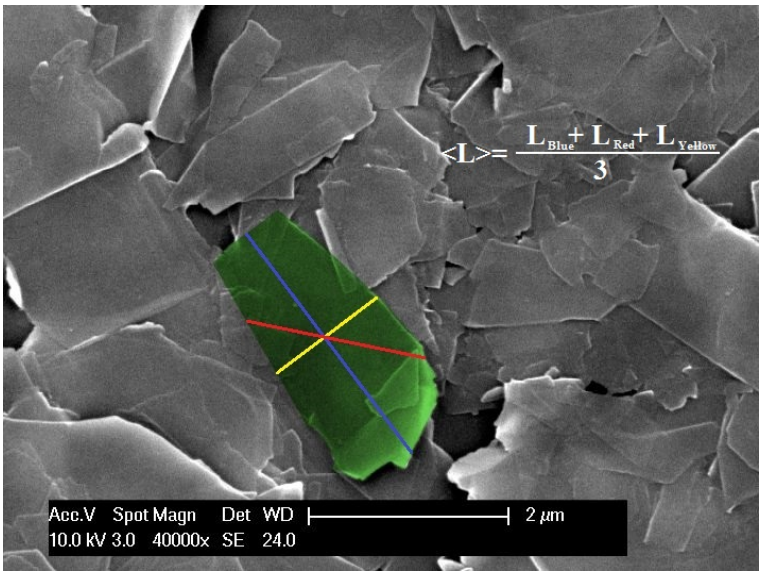

Figure 2.3: Top view SEM image of graphene laminate on PET. The intersecting lines were used for determing the average flake size

of overlapping single layer graphene and FLG flakes with different sizes and shapes. For statistical analysis, extensive top view SEM studies have been performed to determine an average flake size D of a large number of flakes. The average flake size is defined as an average of the three diameter of each flake (see Fig. 2.3). To achieve sufficient accuracy for statistical calculation of D, more than hundred flakes have been taken into consideration for each sample. Fig. 2.4 shows the statistical analysis results for sample 1, 4 and 6. It has been noticed that after almost ~ 50 flakes are included in the analysis the average size saturates to a particular well-defined value [1]. All the values of average flake size have been provided in Table 2.1.

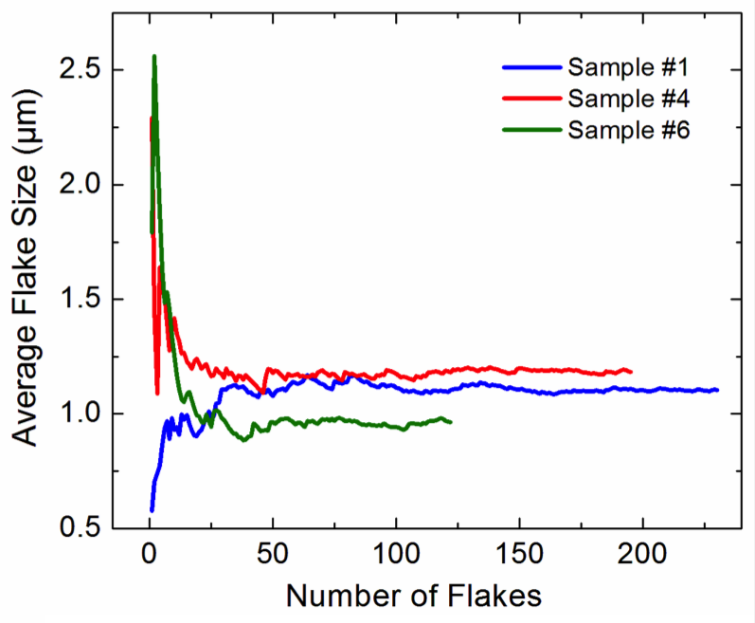

Figure 2.4: Statistical analysis of the FLG flake size in GL-on-PET samples. The calculated average flake size is shown as a function of the number of flakes taken into account. The data is presented for the uncompressed (sample 1) and two compressed (samples 4 and 6) GL-on-PET. Note that the flake sizes converge to the asymptotic average values of 1.10, 1.18 and 0.96 after number of the accounted flakes exceeds about a hundred. The figure is reproduced from H. Malekpour, K. H. Chang, J. C. Chen, C. Y. Lu, D. L. Nika, K. S. Novoselov, A. A. Balandin, *Nano Lett.* **14**, 5155 (2014) with permission from American Chemical Society.

2.3 Optothermal Raman measurements of thermal conductivity

For thermal studies of GL, the non-contact optothermal Raman (OTR) method was used [10]. OTR is a direct steady-state measurement technique that determines the value of thermal conductivity directly, without any need to calculate it from diffusivity value. This technique was originally introduced by Balandin and co-workers for measuring thermal properties of single layer graphene [7]. The measurement technique includes micro-Raman spectrometer, which is used as thermometer to determine the local temperature rise. The Raman excitation laser also serves as a heater to induce local heating in the sample. Owing to the clear G-peak Raman band of graphene, the temperature could be accurately read. The measurement procedure involved two steps: the calibration measurement and the power-dependent Raman measurement. More details of OTR technique can be found in chapter 1. Here micro-Raman analysis was performed using 488 nm excitation wavelength and power level varying up to 10 mW. For power-dependent Raman measurement, the GL-on-PET samples were cut into the rectangular ribbons and suspended across a specially designed sample holder, shown in Fig. 2.5. The sample holder contains two massive aluminum clamps serving as ideal heat sinks and providing good thermal contact with GL layers.

The calibration measurement was performed inside a cold-hot cell. The cold-hot cell allows the temperature of the sample to be controlled externally. Low excitation power of the Raman laser ($\sim 1mW$) was maintained during calibration measurement to avoid laser-

induced heating. As a result of the calibration, the Raman G peak position is determined as a function of the temperature of the sample. Here the temperature interval of $20°C - 200°C$ was used. It has been noticed that the G peak position followed an excellent linear shift over the examined temperature range. The slope determines the temperature coefficient of G Raman peak, χ_G, for the measured temperature range. One should note that the χ_G value depends not only on the sample properties but also on the temperature range for which it was extracted.

The second part of OTR method, power-dependent Raman measurement, includes recording the position of Raman G peak as a function of the increasing excitation laser power using the special designed sample holder described earlier. The power on the sample surface was measured by replacing the sample with a photodiode power sensor. The increase in the absorbed laser power, ΔP, generates local heating leading the Raman G peak to red shift ($\Delta\omega$). The shift over G peak was recorded for the uncompressed and compressed samples as the function of the absorbed power. Having the sample geometry and temperature rise, $\Delta T = {\chi_G}^{-1}\Delta\omega$, in response to the absorbed power, ΔP, thermal conductivity K can be extracted by solving the heat diffusion equation numerically. Fouriers equation was solved for the specific sample geometry. Considering the large thickness of GL layer ($\sim 9\mu m$ $\sim 44\mu m$), the heat diffusion equation needs to be solved in 3-D structure. COMSOL software package was used for numerical solution of the equation with proper boundary conditions. Details of K extraction procedure is provided in chapter 1. A Gaussian distribution of power with the standard deviation set to the laser spot size was used to simulate the laser induced heating. The suspended GL-on-PET ribbon is connected to the heat sinks at its two ends,

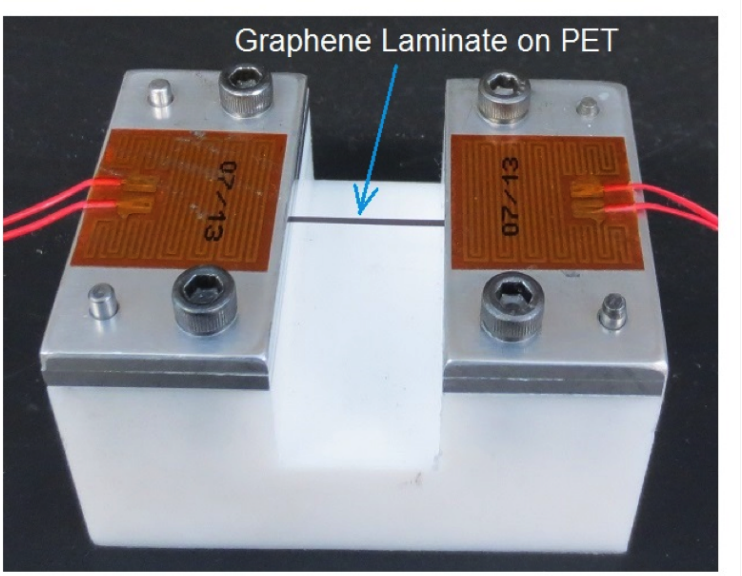

Figure 2.5: Optical image of the specially designed sample holder for optothermal Raman measurements with macroscopic thin films. The GL-on-PET sample under test (seen as gray ribbon) is suspended across a trench and fixed with two massive aluminum pads acting as the heat sinks. The ribbon is heated with the Raman laser in the middle. The experimental setup is a scaled up version of the original one used for the measurement of the thermal conductivity of graphene. The figure is reproduced from H. Malekpour, K. H. Chang, J. C. Chen, C. Y. Lu, D. L. Nika, K. S. Novoselov, A. A. Balandin, *Nano Lett.* **14**, 5155 (2014) with permission from American Chemical Society.

modeled as being at RT. All other boundaries are defined as insulated from the environment, modeled by having a zero temperature gradient across the boundary. An iteration strategy was used to solve the heat diffusion equation. The total power and the thermal conductivity were given as the inputs to the equation and the temperature distribution is determined as the result of simulations. The temperature rise is then compared with the measured temperature and based on the results the thermal conductivity is adjusted to higher or lower value.

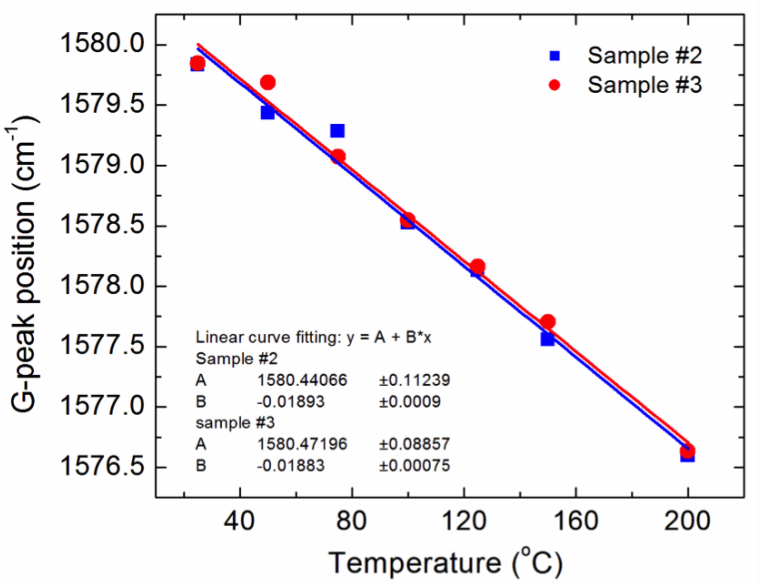

Figure 2.6: Raman G peak as a function of the sample temperature. The measurements were carried out under the low excitation power to avoid local heating while the temperature of the sample was controlled externally. Note an excellent liner fit for the examined temperature range. The obtained dependence is used as a calibration curve for the thermal measurement. The figure is reproduced from H. Malekpour, K. H. Chang, J. C. Chen, C. Y. Lu, D. L. Nika, K. S. Novoselov, A. A. Balandin, *Nano Lett.* **14**, 5155 (2014) with permission from American Chemical Society.

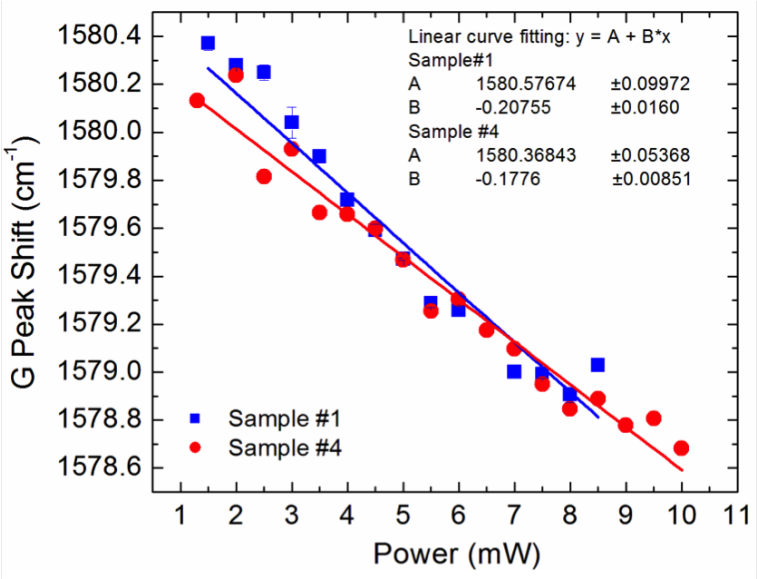

Figure 2.7: Raman G peak shift as a function of the laser power on the sample surface. The results are shown for the uncompressed (sample 1) and compressed (sample 4) GL-on-PET. The shift in G peak position with increasing power indicates the local temperature rise. The slope of these linear dependencies is used for the extraction of the thermal conductivity. The figure is reproduced from H. Malekpour, K. H. Chang, J. C. Chen, C. Y. Lu, D. L. Nika, K. S. Novoselov, A. A. Balandin, *Nano Lett.* **14**, 5155 (2014) with permission from American Chemical Society.

2.4 Effect of the flake size on thermal conductivity of laminate

2.4.1 Experimental results

Following the procedure described in the previous section, the room temperature thermal conductivities were measured for different uncompressed and compressed GL-on-PET and is shown in Fig. 2.8 and summarized in Table 2.1. One can see from Fig. 2.8 that the overall thermal conductivity values for GL-on-PET are pretty high ~ 40 W/mK 90 W/mK. Considering the extremely low thermal conductivity of PET and related plastic materials ($K \approx 0.15$ W/mK - 0.24 W/mK), coating PET with graphene laminate enhances the thermal conductivity by more than two orders of magnitude (up to ×600 times). Based on the plotted results (Fig. 2.8) high values of thermal conductivity can be obtained in both compressed and uncompressed GL. No correlation was noticed between thermal conductivity of GL and its mass density or thickness. It was found interestingly that thermal conductivity of both uncompressed and compressed GL scales linearly with the average flake size D. This would suggest that heat conduction in GL layers is limited by the flake boundaries rather than intrinsic properties of the graphene and FLG. Compression improves the flakes alignment and consequently results in higher K value at a given flake size. The better alignment between flakes was confirmed by top view SEM analysis of the flakes, which suggests the population of vertically oriented flakes is suppressed in the compressed samples. The misaligned flakes appear as bright white spots (see Fig. 2.1). In order to theoretically interpret the experimental results, the theory of heat transfer in FLG was applied. This

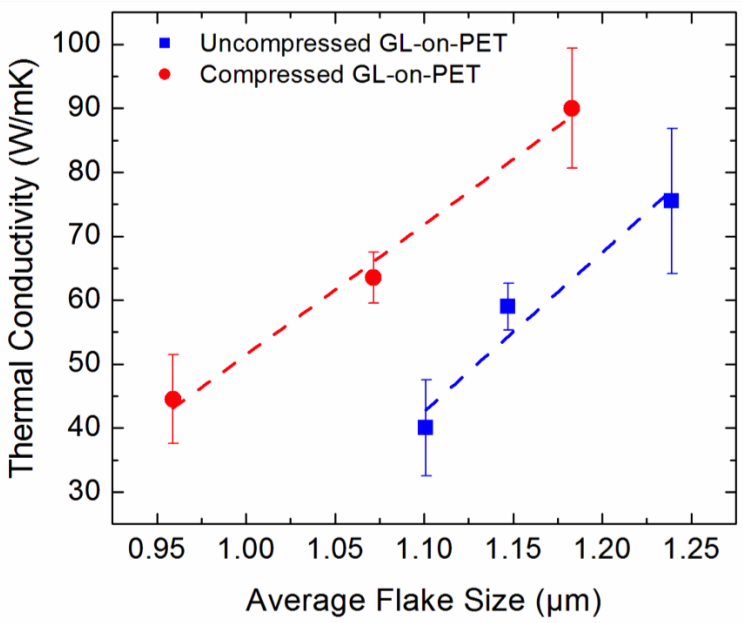

Figure 2.8: Thermal conductivity of GL-on-PET as a function of the average flake size D. The results are shown for the compressed (red circles) and uncompressed (blue rectangles) GL-on-PET samples. The dashed lines are to guide the eyes only. Note that the high thermal conductivity can be achieved in both uncompressed and compressed samples. For the same flake size D, the compressed samples have higher thermal conductivity than uncompressed ones owing to better flake alignment. The figure is reproduced from H. Malekpour, K. H. Chang, J. C. Chen, C. Y. Lu, D. L. Nika, K. S. Novoselov, A. A. Balandin, *Nano Lett.* **14**, 5155 (2014) with permission from American Chemical Society.

will be discussed in the next section.

2.4.2 Theoretical analysis

Heat conduction in GL-on-PET in the plane direction consists of heat distribution in individual flakes and their boundaries conduction. Therefore, the total in-plane thermal conductivity depends on thermal conductivity of each FLG flake as well as the strengths of their coupling to each other. Defining a theoretical thermal conductivity to GL with such a random structure is not easy due to uncertainty of parameters like the strength of

individual flakes attachment and their mutual orientation. In order to gain insight into the heat conduction in graphene laminate, formulas describing heat conduction in graphite thin film were modified [11, 12]. The specifics of graphene laminates that are entered to the model are characteristic dimensions of the flakes and concentration of defects. The thermal conductivity in graphene laminates for its basal plane is written as [11, 13, 14]:

$$K = K_{xx} = \frac{1}{L_x L y L z} \sum_{s,q} h\omega_s(\vec{q})\tau(\omega_s(\vec{q}))v_{x,s}v_{x,s}\frac{\partial N_0}{\partial T} \tag{2.1}$$

Where $\tau(\omega_s(\vec{q}))$ denotes the relaxation time of a phonon with the frequency $\omega_s(\vec{q})$ from the s-th acoustic phonon branch ($s = LA, TA, ZA$), $\vec{q} = (q_\parallel, q_z)$ is the phonon wave vector, $v_{x,s}$ is the projection of phonon group velocity, N_0 is the Bose-Einstein distribution function, T is the temperature and L_x, L_y, L_z are the actual sample size. The terms LA, TA and ZA show the longitudinal acoustic, the transverse acoustic and the out-of-plane acoustic phonon branches, correspondingly. Following the approach described in Ref. [11] the phonon transport in GL is defined to be two-dimensional (2D) for phonons with frequencies $\omega_s > \omega_{c,s}$ and three-dimensional (3D) for phonons with frequencies $\omega_s \leq \omega_{c,s}$, where ω_c is a certain low-bound cutoff frequency. Applying the equal-energy surfaces approximation with the cylindrical surfaces, one can rewrite Eq. 2.1 for the 2D and 3D parts of the thermal conductivity in the following form [11]:

$$K^{3D} = \frac{\hbar^2}{4\pi^2 K_B T^2} \sum_{s=LA,TA,ZA} \frac{1}{V_s^\perp} \int_0^{\omega_{c,s}} [\omega_s^\parallel(q_\parallel)]^3 \tau(\omega_s^\parallel) v_s^\parallel(q_\parallel) \frac{exp(\frac{\hbar\omega_S^\parallel}{K_B T})}{[exp(\hbar\omega_S^\parallel) - 1]^2} q_\parallel d\omega_s^\parallel \tag{2.2}$$

$$K^{2D} = \frac{\hbar^2}{4\pi^2 K_B T^2} \sum_{s=LA,TA,ZA} \frac{\omega_{c,s}}{V_s^\perp} \int_{\omega_{c,s}}^{\omega_{max,s}} [\omega_s^\parallel(q_\parallel)]^2 \tau(\omega_s^\parallel) v_s^\parallel(q_\parallel) \frac{exp(\frac{\hbar\omega_S^\parallel}{K_B T})}{[exp(\hbar\omega_S^\parallel) - 1]^2} q_\parallel d\omega_s^\parallel \tag{2.3}$$

where $v_s^{\perp} = \omega_{c,s}/q_{z,max}$ and $\omega_{c,s}$ is the phonon frequency of s-th branch at Apoint of graphite Brillouin zone.

In these calculations three mechanisms of phonon scattering were taken into consideration [12–15]: Umklapp scattering $\tau_U(\omega_s^{\parallel}) = M{v_s}^2\omega_{max,s}/(\gamma_s^2 K_B T[\omega_s^{\parallel}]^2)$, point-defect scattering $\tau_{pd}(\omega_s^{\parallel}) = 4v_s^{\parallel}/(S_0\Gamma q[\omega_s^{\parallel}]^2)$ and scattering on the flake boundaries $\tau_b(\omega_s^{\parallel}) = D/v_s^{\parallel}$, where the average Gruneisen parameter is branch dependent and is equal to $\gamma_{LA} = 2$,$\gamma_{TA} = 1$,$\gamma_{ZA} = -1.5$, $\omega_{max,s}$ is the maximal frequency of s-th branch, S_0 is the cross-section area per atom, M is the graphene unit cell mass and Γ is a parameter showing the strength of the point-defect scattering and defined from the typical defect densities in the given material. Here τ is the total phonon relaxation time determined from the Matthiessens rule $1/\tau = 1/\tau_{pd} + 1/\tau_U + 1/\tau_b$.

In this model the scattering from the boundaries of FLG was assumed to be completely diffused. The low-bound value of Γ parameter was estimated from the energy-dispersive X-ray spectroscopy (EDS). The EDS results show the characteristic material composition 92% - 94% of Carbon, 5.7% - 6.5% of Oxygen, 0.34% of Sodium and 0.56% of Sulfur. Using these impurity composition, the parameter is calculated to be 0.02-0.03. This value does not take into account the effect of vacancies and related structural defects, which also contribute to the phonon-point defect scattering. Therefore, larger Γ values in the range 0.05-0.2 were used. This value is rather typical for semiconductor or electrically insulating technologically important materials.

The results of their calculations is shown in Fig. 2.9 (a-b) demonstrating the dependence of the thermal conductivity $K = K^{3D} + K^{2D}$ on the temperature for different

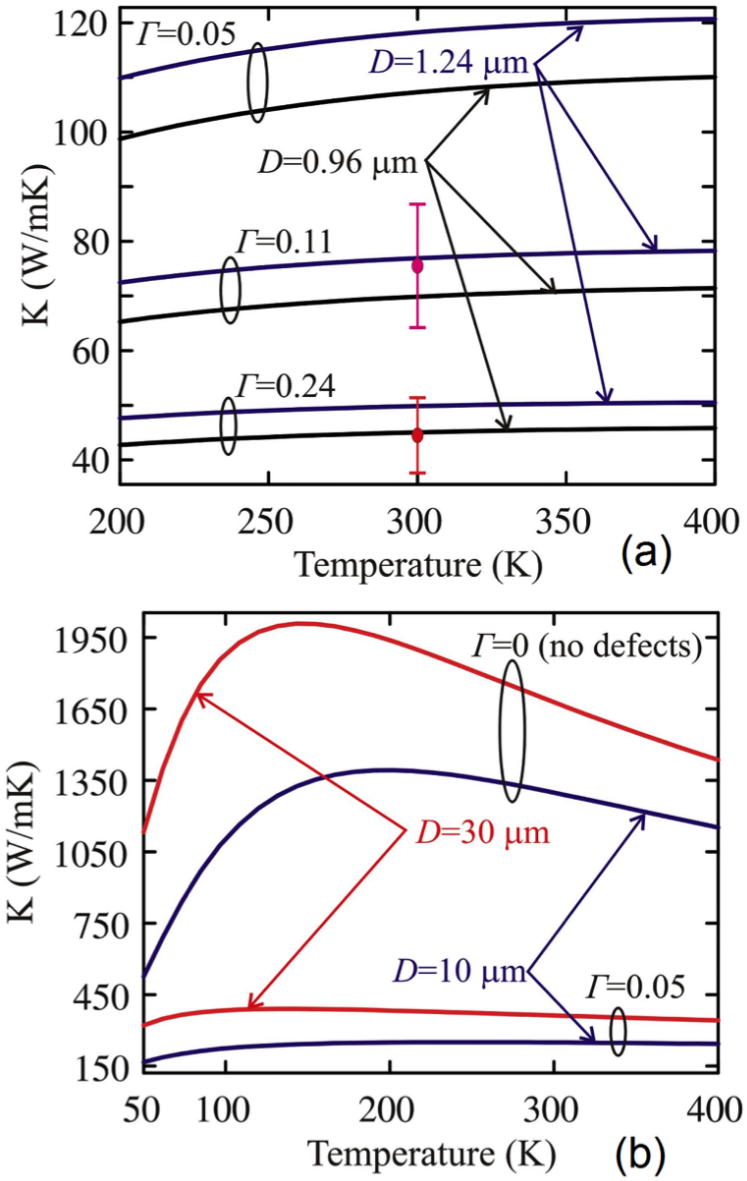

Figure 2.9: Calculated thermal conductivity as a function of temperature shown for different flake size D and defect scattering strength Γ. Not that increasing D or decreasing Γ increases the thermal conductivity and strengthens its temperature dependence. The experimental data points are shown with the circles. The figure is reproduced from H. Malekpour, K. H. Chang, J. C. Chen, C. Y. Lu, D. L. Nika, K. S. Novoselov, A. A. Balandin, *Nano Lett.* **14**, 5155 (2014) with permission from American Chemical Society.

values of the average flake size D and different Γ. For comparison the experimental points have been added to the plot, depicted by the red and pink circles. A weak dependence of K on the temperature was noticed in the range of experimentally observed values of K. The same behavior was observed in polycrystalline materials, where the phonon scatterings on crystalline grains dominate [15]. One should note that increasing D or decreasing Γ, leads to restoration of the strong dependence of K on the temperature (see Fig. 2.9 (a)). This behavior is typical for the crystalline semiconductors and graphene [16]. It was found that the dependence of K on D obtained from calculations is weaker than that of experimental one. This inconsistency was attributed to different orientation and coupling of flakes in experimental samples, which has not been considered in the model description. The increasing dependency of thermal conductivity with the increasing size of the graphene fillers, that was observed experimentally, was successfully conformed by theoretical calculations. This dependency is in line with the literature reports for carbon nanotubes and other carbon allotropes [17, 18]. The values of the thermal conductivity obtained for graphene laminate at RT ($K \sim 90\ W/mK$) are significantly lower than measured values reported for large suspended graphene layers ($K \sim 3000\ W/mK$) [10]. This smaller value was explained by the fact that the thermal conductivity of the laminates is limited not by the lattice dynamics of the graphene flakes but by their size, flake coupling and orientation with respect to the heat flux.

Chapter 3

Free standing reduced graphene oxide film

Due to its extremely high in-plane thermal conductivity, graphene inspired a surge in experimental and theoretical studies of heat conduction in graphene and other two-dimensional (2-D) materials [11, 14, 19–22]. The thermal conductivity of graphene can exceed that of the basal planes of graphite [7, 10, 23–25]. Both graphene and few-layer graphene (FLG) have been proposed as fillers in the thermal interface materials [26–28]. Moreover, they can be useful as flexible heat spreaders for cooling local hot spot in electronics and optoelectronics [1, 29–31]. For this reason, researchers are trying to develop methods to scale up the production of graphene sheets. One of the possible procedures to industry-scale applications of graphene-based materials for thermal management is the reduction of graphene oxide (GO). However, the quality of graphene sheet produced by this technique is lower

compared to the theoretical potential of pristine graphene and compared to other methods such as mechanical exfoliation. This cost effective lower quality graphene can still be useful for applications, such as thermal management, where exploiting high intrinsic electrical and thermal properties of graphene is not critical. In this section the properties of chemically treated reduced graphene oxide (rGO) films have been investigated. The GO films have been chemically reduced using Hydroiodic Acid (HI) and then further annealed at $300°C$. Both the in-plane and cross-plane thermal conductivities were measured using a combination of two different techniques: Raman opto-thermal and laser flash. The details of the studied samples will be discussed in the following section.

3.1 Reduction of freestanding graphene oxide film

Graphene [32] and few-layer graphene (FLG) are well known for their excellent thermal conduction properties [7, 10, 23–25]. They have been demonstrated as ideal filler for thermal interface materials (TIMs) [26–28], lateral heat spreaders [33], graphene coating and laminates [1]. Despite the high thermal conductivity of exfoliated and deposited graphene, 2000-5000 W/mK [7, 10, 34–36], it cannot be used for practical thermal management applications, since it does not have the industrial requirements. For practical applications, it is important to develop a cost effective procedure, producible in large scale and suitable for batch processing. The restoration of graphene from reduction of graphene oxide [37] is a promising method for industry scale synthesis of graphene for thermal management applications. This is mainly due to the fact that graphene oxide is strongly hydrophilic and thus the exfoliation of graphene oxide from graphite oxide is eased. However, the quality

of the produced graphene, reduced graphene oxide, is lower than graphene produced by mechanical exfoliation and other techniques like MBE and CVD.

Graphite oxide, which is a compound of carbon, oxygen and hydrogen, is artificially created by treating graphite with strong oxidizers. The Hummers method and its modifications [38, 39] have been established as a successful method for mass production of GO from natural graphite. However, very low values of thermal conductivity ~ 2.9 W/mK have been reported for GO produced by this technique [33]. Graphene oxide is therefore reduced using different chemical and thermal reduction methods [40] all aiming to restore graphene lattice structure and its excellent electrical and thermal characteristics. Among the whole process of oxidation and reduction, reduced graphene oxide is exposed to damages, residue and impurities, all lowering the quality of produced graphene. Thus, for practical applications it is important to understand how the reduction process affects the heat conduction in rGO films.

The samples for this study were provided by university of Manchester. The thermal and electrical properties of three different types of rGO films have been investigated. The GO film has been chemically reduced using Hydroiodic Acid (HI) and then further annealed at 300 $°C$. Two samples of each reduction procedure have been studied. Due to the random nature of air packet formation, their appearance is different in each same-type sample and thus the two samples have different morphology. More details of the samples are shown in Table 3.1.

Table 3.1: Samples description and details

Sample ID	Thickness $[\mu m]$	Density $[g/cm^3]$	Description
GO	12.6	1.83	Pristine graphene oxide membrane
HI-1	13.3	1.69	Hydro Iodic acid reduced GO
HI-2	15.8	0.65	
HI-300-1	89.3	0.15	Hydro Iodic acid reduced GO further annealed at 300 °C
HI-300-2	27.9	0.20	
LSHI-300-1	310	0.02	Large GO flakes reduced with Hydro Iodic acid and further annealed at 300 °C
LSHI-300-2	12.3	0.18	

3.2 Characterization of free standing reduced graphene oxide films

Different characterization techniques were used to determine the effect of reduction on the film properties:

1. Scanning electron microscopy (SEM) to study the effect of reduction on microstructure of the samples.

2. X-ray photoelectron spectroscopy (XPS) to study the effect of reduction on carbon to oxygen atomic ratios.

3. Electrical conductivity as a criterion of the effectiveness of reduction.

4. Ultra violate (UV) and visible Raman spectroscopy to study sp2/sp3 carbon bonding and defects in reduced films.

3.2.1 Scanning electron microscopy

SEM has been performed on the samples surface and cross section in order to better understand their microstructure (see Fig. 3.1). Fig. 3.1 (a-c) shows the top view and (d-i) shows the cross section SEM images of the rGO films. The cross section SEM images show the layered structure of the films. However, after thermal treatment, due to the release of oxygen and carbon dioxide, air packets form in between layers and results in the increase of film thickness and thus the decrease in density (see Table 3.1). As depicted in Fig. 3.1 (a-c), after both thermal and chemical treatment, the surface of reduced GO forms a rough and corrugated structure due to the air packets trapped in the underneath layers. The morphological changes seen in SEM confirm the thickness and density values provided in 3.1. The thickness H = 12.6 μm of the reference GO film increased to H = 13.3 μm after chemical treatment using Hydroiodic acid and then significantly increased to H = 89.3 μm after thermal treatment at 300 $^{\circ}C$. In consequence, the apparent mass density decreases from 1.83 gr/cm^3 in GO reference sample all the way down to 0.15 gr/cm^3, after both chemical and thermal treatment, which is in line with previous reports [33]. The formation of air packets strongly affects the cross-plane thermal transport while not seriously affecting the in-plane thermal conduction.

3.2.2 X-Ray photoelectron spectroscopy

Depending on its preparation technique, GO can have chemical compositions ranging from $C_8O_2H_3$ to $C_8O_4H_5$, which corresponds to a carbon to oxygen ratio (C/O) of 4:12:1 [41–43]. After reduction, this ratio is typically increased to approximately 12:1 [44, 45]. In

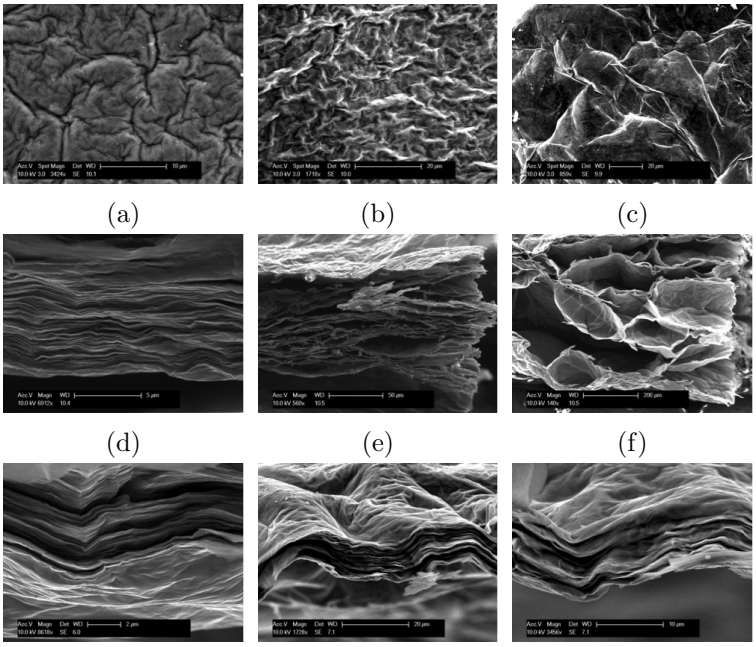

Figure 3.1: Scanning electron microscopy of top view (a) HI-1 (b) HI-300-1(c) LSHI-300-1 and cross section view (d) HI-1(e) HI-300-1(f) LSHI-300-1(g) HI-2(h) HI-300-2 (i) LSHI-300-2 free standing rGO films. After thermal treatment, air bubbles form and the structures become more corrugated. Do to the random nature of this process, each sample possess its own microstructure and morphology.

Table 3.2: XPS elemental compositions and extracted Γ parameter

Sample ID	C1S [%]	O1S [%]	I3d [%]	Si2p [%]	Al2p [%]	Γ
GO	58.8	23.5	0.0	17.7	0.0	-
HI-1	80.1	15.8	0.5	2.6	1.0	1.287
HI-2	85.1	13.9	0.4	0.6	0.0	0.853
HI-300-1	87.7	11.4	0.3	0.0	0.6	0.647
HI-300-2	85.9	12.5	0.4	1.2	0.0	0.854
LSHI-300-1	82.7	15.7	0.3	0.6	0.7	0.824
LSHI-300-2	83.3	12.3	0.5	3.9	0.0	1.188

order to investigate the effectiveness of the reduction, X-Ray Photoelectron Spectroscopy (XPS) was used to extract chemical composition of the samples. All samples show Carbon (C), Oxygen (O) and Silicon (Si) elements with different concentrations. After chemical reduction, Aluminum (Al) and Iodine (I) also appears in XPS data. More details of the elemental concentration can be found in Table 3.2. In order to investigate the functional groups of the films, the XPS C1s peaks were curve-fitted by its components. The main peaks of the reference GO sample occurs at ~ 284.9 eV and ~ 287.2 eV corresponding to sp^3 Carbon and double bonded Carbon-Oxygen (C=O), respectively. As the reduction goes on, C=O bonding disappears and low intensity peaks at ~ 286 eV and ~ 288.8 eV evolves, which corresponds to single bonded Carbon-Oxygen (C-O) and single/double bonded Carbon-Oxygen combination (O-C=O) (See Fig. 3.2). Moreover, sp^2 Carbon peaks appears at ~ 285 eV after chemical/thermal treatment confirming the gradual restoration of the graphene structure. The removal of Oxygen by chemical/ thermal treatment leads to the carbon concentration to increase from ~ 59% in GO up to ~ 88%. The reported XPS data for GO and rGO are in agreement with previous reports showing Carbon sp^2 peak energy in the

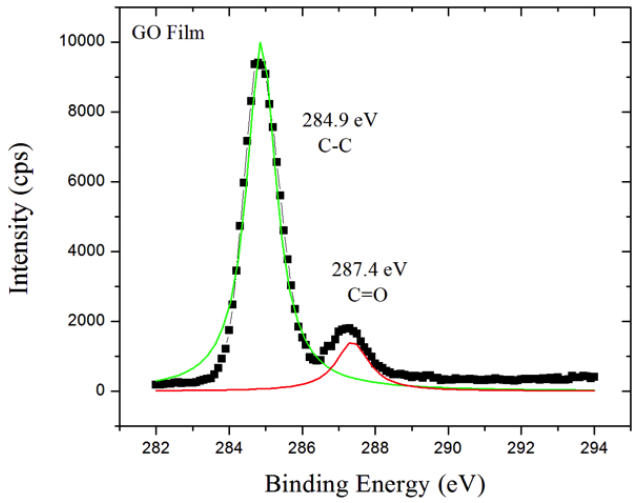

(a)

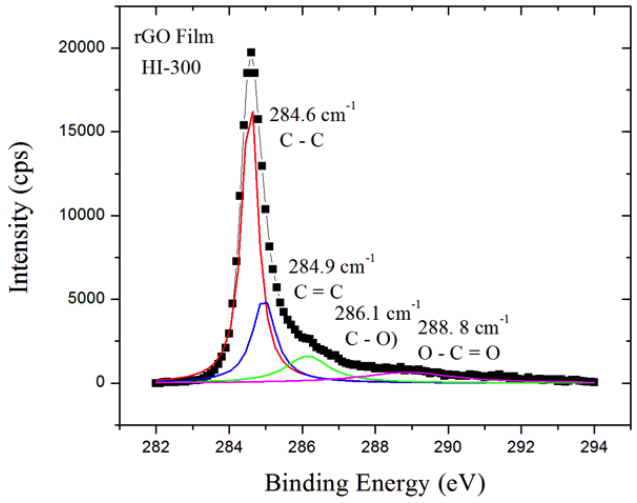

(b)

Figure 3.2: X-ray photoelectron spectroscopy data of the carbon C1s signatures of (a) reference graphene oxide film and (b) HI-300-1. Lorentzian curve fitting was done and the main peaks of GO occurs at ~ 284.9 eV and ~ 287.2 eV corresponding to sp^3 Carbon and double bonded Carbon-Oxygen (C=O). C=O bonding disappears after the reduction and instead low intensity peaks at ~ 286 eV and ~ 288.8 eV corresponding to single bonded Carbon-Oxygen (C-O) and single/double bonded Carbon-Oxygen combination (O-C=O) evolves.

range $284.1 - 285\ eV$ while Carbon sp^3 peak energy in the range $284.9 - 286\ eV$ [46–50].

3.2.3 Electrical conductivity

Another parameter that is used to qualitatively estimate the effectiveness of reduction is films electrical conductivity. GO by itself has very high sheet resistance, $\sim 0.5\ M\Omega/\square$ [33]. Significant increase in electrical conductivity has been reported for reduced GO films [33, 51–55], attributed to the enhancement of carbon sp^2 phase [33, 49]. Here in this study, electrical conductivity was measured for both GO and rGO films using two probe technique. It was found that our chemical reduction technique followed by thermal annealing results in electrical conductivity to increase significantly from $\sim 1.2 \times 10^{-5}\ S/cm$ to $\sim 0.6 - 25.4\ S/cm$. The results are compatible with previous reported values [33].

3.2.4 Raman spectroscopy

Raman spectroscopy is another characterization technique that is used to better investigate the structure and composition of the GO and rGO films. Raman spectroscopy (Renishaw InVia) was performed in a backscattering configuration under visible ($\lambda = 488\ nm$) and UV ($\lambda = 325\ nm$) laser excitations. Fig. 3.3 shows the Raman spectra of GO and reduced GO films after chemical and thermal treatment (sample HI-300-1). The peaks at $\sim 1350\ cm^{-1}$ and $\sim 1580 cm^{-1}$ in rGO visible Raman spectrum correspond to D and G band, respectively. However the G-band of GO reference sample is instead a broad non-symmetric peak centered at $\sim 1590\ cm^{-1}$. As the reduction goes on, this broad band splits into two symmetric bands at $\sim 1580\ cm^{-1}$ and $\sim 1620\ cm^{-1}$ correspond to G and D bands, respectively. The 2D band at $\sim 2700\ cm^{-1}$ and the S3 band near $\sim 2900\ cm^{-1}$ are also present in Raman spectrum,

which confirms previous reports [56–58]. The S3 band is known to be due to the second-order of a combination of D and G bands [59]. After reduction, the 2D band becomes more prominent. On the other hand, in UV Raman spectra of both GO and rGO films, the 2D band is quenched, while the G-band remains strike and keeps its position. Moreover, the ratio of Raman D to G band reduces under UV Raman as expected, since this ratio not only depends on defects but also varies with excitation wavelength [60]. Having both UV and visible Raman spectra helps us evaluate sp^2 and sp^3 carbon content, qualitatively. This is due to the fact that UV Raman is more sensitive to sp^3 carbon and Carbon-Hydrogen C-H bonding.

The intensity ratio of the Raman D to G bands (I_D/I_G) reveals interesting behavior and is of interest. Raman D to G peak intensity ratio is a measure of disordered carbon, indicated by the sp^3/sp^2 carbon ratio [61]. A linear rise in I_D/I_G has been observed with increasing electrical condutivity in ref.[51]. This intensity rise indicates that the crystallinity of the materials is degrading. Due to reduction the average size of sp^2 domain decreases but the number of these domains increases leading to the intensity ratio of D to G Raman band to increase [62]. However some groups reported a non-monotonic behavior of this intensity ratio (first increase and then decrease), which could be attributed to the restoration of the graphitic network due to healing [50]. Fig. 3.4 shows the behavior of different Raman parameters with the degree of reduction. The XPS carbon concentration has been used to represent the degree of reduction. As the reduction proceeds, the D to G peak intensity ratio shows a non- monotonic behavior, initially increases and then decreases (Fig. 3.4 (b)). However, the D peak width constantly decrease from ~ 136 cm^{-1} all the way down to ~ 60

cm^{-1} (Fig. 3.4 (a)). These results are in line with previous reports, which suggested to use D-peak width as a measure of reduction degree [50]. The monotonic decrease on Raman D peak width with reduction is interpreted by the restoration of the graphene interatomic distances and angles and to the smoothening of the films [50].

3.3 Thermal conductivity of free standing reduced graphene oxide film

The in-plane and cross-plane thermal conductivities of the films have been measured using a combination of two different techniques: Opto-Thermal Raman (OTR) method and Laser Flash Technique (LFT). Due to the anisotropic thermal transport behavior of these layered films, the cross-plane thermal conductivity value is needed in order to extract the in-plane thermal conductivity using OTR measurement. As discussed in chapter 1, OTR is a direct measuring technique originally introduced for measuring thermal conductivity of single layer graphene [7]. The method was later developed for macro scale size samples using special designed sample holder [1]. OTR is a steady state measuring technique in which the thermal conductivity is directly measured without any need to be calculated from diffusivity value. In this non-contact technique, the micro Raman spectrometer acts both as a heater and thermometer. The Raman excitation laser causes local heating on the sample. This local heating is then measured using Raman spectrometry, following the two steps procedure: The calibration measurement and the power-dependent Raman measurement. The micro-Raman spectroscopy (Renishaw In Via) was performed under 488 nm excitation laser

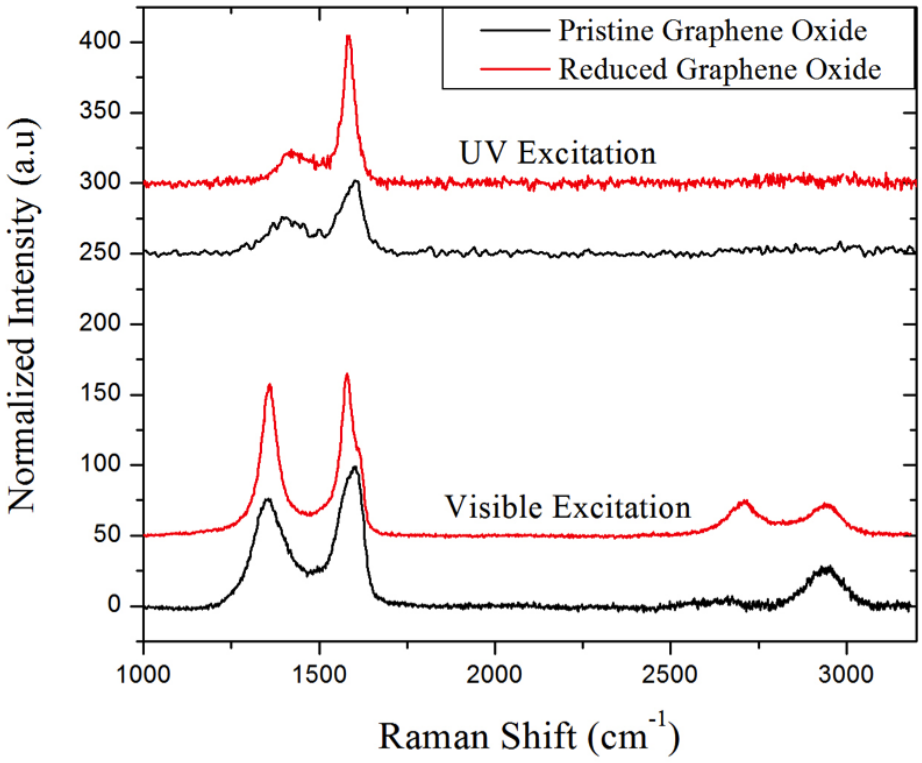

Figure 3.3: Raman spectra of GO and rGO (HI-300-1) films under visible (488 nm) and UV (325 nm) excitation wavelength. In rGO visible Raman spectrum, the peaks at ~ 1350 cm^{-1} and ~ 1580 cm^{-1} correspond to D and G peak, respectively. The G-peak of GO film is a broad non-symmetric peak at ~ 1590 cm^{-1}, which splits into two overlapping peaks in reduced GO film: G and D. The peaks at ~ 2700 cm^{-1} and ~ 2900 cm^{-1} corresponds to 2D and S3 band. One should notice that 2D band is more intense in reduced GO film. In UV raman spectrum, the D-band appears around ~ 1408 cm^{-1} and ~ 1432 cm^{-1} for GO and rGO films, respectively.

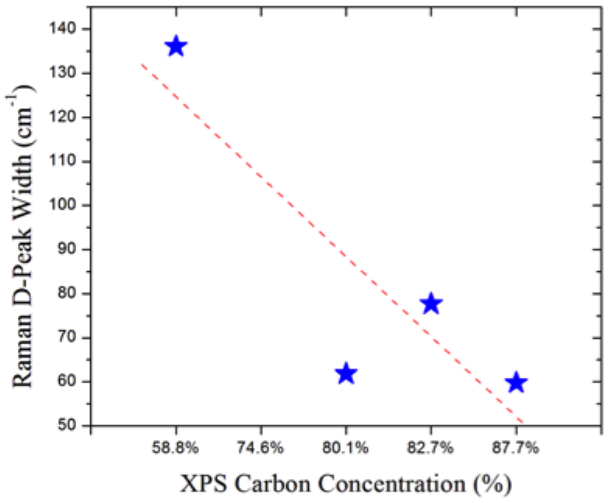

(a)

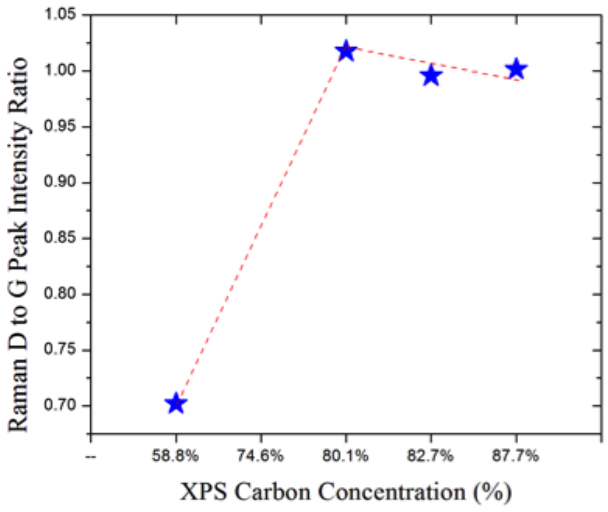

(b)

Figure 3.4: The variation of visible Raman spectrum parameters with XPS carbon concentration, for samples labeled as group 1. XPS carbon concentration was used as a measure of rduction degree: (a) Raman D band width reduces linearly with the reduction degree and (b) Raman D to G band intensity ratio shows a non-monotonic behaviour with the reduction degree.

and power ranging from 1-4 mW. Following our approach for OTR in macro-scale [1], the samples were cut into rectangular ribbons of 1 mm width and suspended across two stainless steel heat sinks, for power-dependent Raman measurement. The calibration measurement was done inside the coldhot cell (LINKAM THMS-600) in which the temperature of the sample is controlled externally. Liquid nitrogen is used in order to achieve below room temperature values. For this study, the temperature range is from $-75°C$ to $125°C$. This temperature range has been selected deliberately to avoid any thermal treatment during OTR measurement. Moreover, in order to avoid local heating during calibration measurement, Raman spectroscopy with low excitation power (below $\sim 1mW$) was performed. At each temperature, three different measurements have been performed in order to achieve an average value. The G-peak position as a function of temperature is then measured during calibration measurement. Fig. 3.5 shows the calibration measurement performed on sample HI-2. A good linear fit has been achieved over the experimental temperature range and the calibration slope of -0.026 cm^{-1}/K has been obtained which is in line with previous reported values for carbon based materials [63]. One should note that the calibration slope depends on both the sample properties and the temperature range.

In the second step of OTR measurement, which is the power-dependent Raman measurement, Raman spectrum is recorded at different laser powers and the shift over G-peak is measured as a function of increasing excitation power. Since these samples are thick enough, it can be assumed that the total laser power impinging on the samples surface is absorbed by the sample and no power is transmitted through the thickness. The laser power on the sample is measured by photodiode power sensor (OPHIR). As the laser power

increases, , the induced local heating increases on the sample, which leads to the G band to red shift. Fig. 3.6 shows the G peak shift with increasing excitation power for sample HI-1 and HI-300-1. As depicted, these two samples with different microstructure and elemental composition, shows different temperature rise to the same excitation power levels. The details of our OTR measurement including the power-dependent slopes and the calibration slopes, for all the six samples, have been shown in Table 3.3. Thermal conductivity can be obtained from sample temperature rise in response to the absorbed power, by knowing the sample geometry. However, in such anisotropic films, it is necessary to know the value of thermal conductivity through the film thickness in order to extract the in-plane thermal conductivity from OTR results.

Initially, OTR was used in order to measure the in-plane thermal conductivity of suspended single layer graphene, which has a 2D structure. However, for thick samples, 3D heat conduction would occur as the cross-plane thermal conductivity is getting involved. If the sample has isotropic heat conduction nature, OTR method is enough to measure the thermal conductivity. However, in case of anisotropic 3D heat conduction, i.e. the heat conduction in thr rGO films used in this study, the in-plane or cross-plane thermal conductivity can be measured by OTR only when one of them is known. For this reason, here in this study, Laser Flash Technique (LFT) was used in order to measure the cross-plane thermal conductivity, independently. As discussed in chapter 1, LFT is a transient method that measures the thermal diffusivity (α) of the material. The thermal conductivity is then calculated by the following equation: $K = \rho\alpha C_p$, where ρ and C_p represents the density and specific heat, respectively. The apparent mass density of the samples was measured directly

Table 3.3: Thermal and electrical conductivity measurement details

Sample ID	OTR $\Delta\omega/\Delta T$ $[cm^{-1}/K]$	OTR $\Delta\omega/\Delta P$ $[cm^{-1}/mW]$	LFT $K_{cross-plane}$ $[W/mK]$	OTR & LFT $K_{in-plane}$ $[W/mK]$	Electrical Conductivity $[S/cm]$
HI-1	0.035	5.98	0.23	20	1.4
HI-2	0.026	6.34	0.13	15	2.1
HI-300-1	0.044	3.18	-	45	0.6
HI-300-2	0.018	3.16	0.59	11	14.7
LSHI-300-1	0.038	4.70	0.27	29	8.2
LSHI-300-2	0.022	2.19	0.83	23	25.4

by dividing their mass to their volume. The cross-plane α was measured using the LFT in the standard configuration in which the rGO film is heated by a flash lamp from one side and the temperature rise on the opposite side is measured using an IR detector. The specific heat of graphite, which has similar thermal properties and has known tabulated C_p was used in order to calculate thermal conductivity values. Previous works by our group on the on thermally annealed rGO films, reported similar C_p values for graphite [33]. Fig. 3.7 depicts the cross-plane thermal conductivity values plotted as a function of temperature (25 to 75 $^{\circ}C$). One should note that all the cross-plane thermal conductivities are rather small (below $\sim 1\ W/m.K$) owing to the layered structure of the material. However, the behavior of cross-plane thermal conductivity with the reduction mechanism seems to be complicated. After thermal treatment, due to the appearance of air packets, the cross-plane thermal conductivity is expected to decrease [33]. On the other hand, due to the appearance of these air packets, the surface roughness increases leading to corrugated structure to form. As a consequent, thermal conductivity is expected to increase owing to the formation of more touching points between the film layers. Considering the cross-plane SEM images

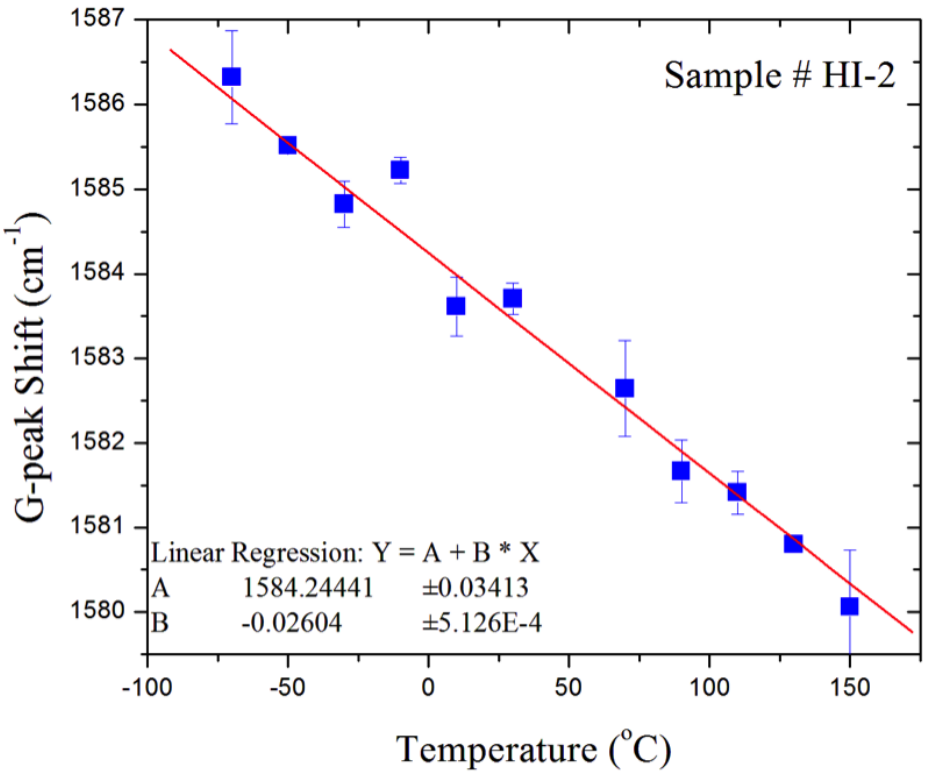

Figure 3.5: Opto-Thermal Raman calibration measurement done on Hydro Iodic acid reduced GO film over the temperature range of -75 °C to 150 °C inside the cold/hot cell. G peak position red shifts linearly as the temperature increase. The slope of this plot is later used to extract thermal conductivity.

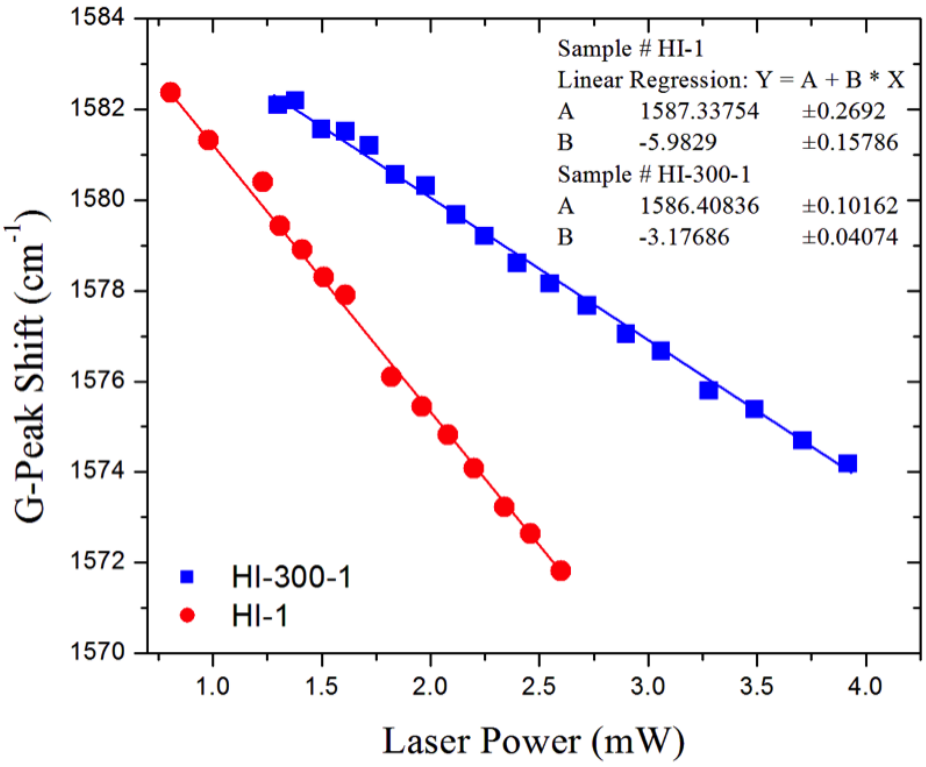

Figure 3.6: Power-dependent Opto-Thermal Raman measurement done on sample HI-1 and HI-300-1 with the excitation power ranging from 1 to 4 mW. The position of Raman Gpeak red shifts linearly as the laser power increases. The difference in the slopes is coming from the different local heating occurred due to the excitation power increase which originates from the difference in thermal conductivities.

depicted in Fig. 3.1, one should note that the most important parameter limiting the cross-plane thermal conductivity is the samples morphology. For example, in the samples labeled as group 2 (HI-2, HI-300-2 and LSHI-300-2), thermal conductivity increases after thermal treatment is applied, originating from more corrugated structure and less air packet formation, compared to group 1. Measuring the cross-plane thermal conductivity of sample HI-300-1 was impossible due to the light penetration through the sample using LFT. In order to later extract the in-plane thermal conductivity of this sample, the anisotropy factor was assumed to be the same as sample LSHI-300-1 which has similar micro-structure to sample HI-300-1. Having cross-plane thermal conductivity values measured by LFT, the in-plane thermal conductivities can be extracted from OTR data. All the in-plane thermal conductivities are shown in Table 3.3. The in-plane thermal conductivity of $\sim 12-40 W/mK$ has been measured for our chemically reduced GO films. However, for the GO reference sample, due to its low thermal conductivity ($\sim 2.9 W/mK$) [33], laser-induced burn occurs even with small excitation powers. Moreover, the broad and non-symmetric Raman G band of GO makes it difficult to do curve fitting and locate the peak position. Therefore, we were unable to extract the thermal conductivity of GO reference sample using OTR technique. Nevertheless, compared to previous reported value for GO film with similar structure (2.9 W/mK) [33], $\sim 4-14$ times improvement of in-plane thermal conductivity has been achieved. The in-plane thermal conductivity seems to be less influenced by the film microstructure and morphology.

Having the in-plane and cross-plane thermal conductivities measured, it is interesting to observe how these values correlate to the films elemental and structural charac-

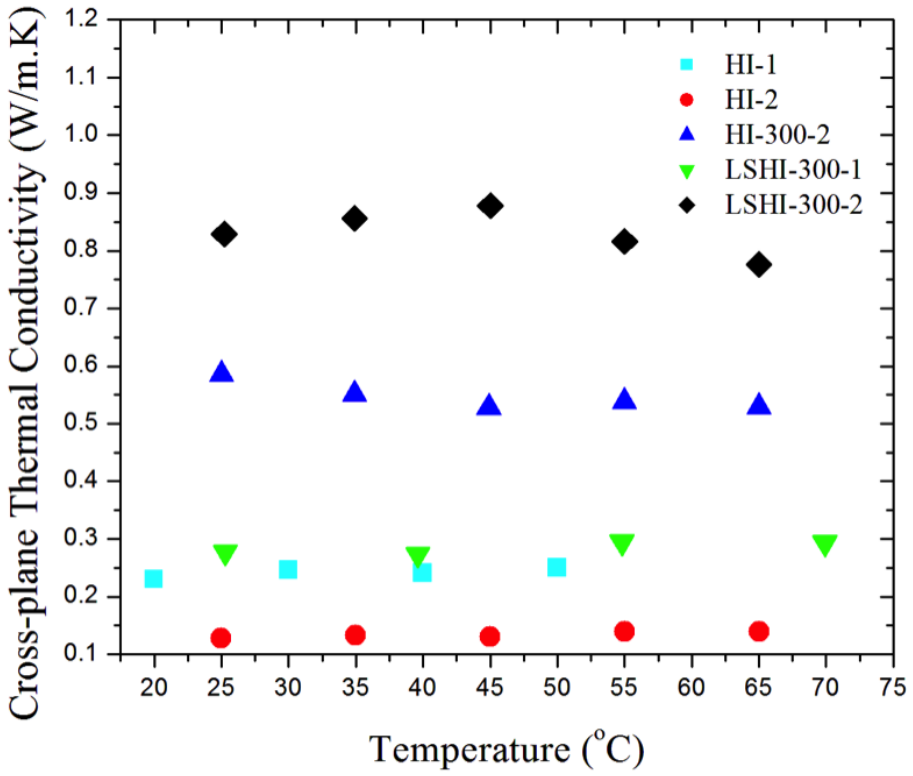

Figure 3.7: Cross-plane thermal conductivity values of graphene oxide and chemically/thermally reduced GO films, obtained using laser flash technique. The Experimental values are plotted as a function of measuring temperature. The cross-plane thermal conductivity is directly affected by the samples microstructure and morphology.

teristics. For this purpose, Raman spectroscopy was used to evaluate the films disorders and carbon hybridization. The behavior of in-plane thermal conductivity versus different Raman parameters has been shown in Fig. 3.8. As the intensity ratio of UV Raman D to G band decreases, thermal conductivity increases almost linearly (see Fig. 3.8 (a)). The decrease in Raman D to G band intensity ratio could correspond to the reduction of defects and sp^3 carbon content, leading to the increase in thermal conductivity. This is also in agreement with previous work [33], reporting a reduction in the UV Raman D to G peak intensity ratio after high temperature annealing of GO film. Full width at half maximum (FWHM) of G band in carbon-based materials, is another parameter which corresponds to the amount of defects and disorders. According to [64], the peak width increases continuously with increasing disorders. In Fig. 3.8 (b), the thermal conductivity is shown as a function of FWHM of G-band for both UV and visible excitation wavelength. It is clearly observed that as a consequence of reduction and graphene restoration, the film disorders will decrease leading to a significant increase in thermal conductivity.

Now that we have both thermal and electrical conductivities, it would be also interesting to compare the electron and phonon contribution in in-plane thermal conductivity. It is known that the thermal transport in graphene is dominated by acoustic phonons [10, 14]. Wiedemann Franz law was used in order to calculate electrical contribution to thermal conductivity and as expected, it was found that more than 99.9% of the conduction is due to phonon transport. The results of our electrical conductivity measurement are shown in Table 3.3. It is interesting to see how the thermal and electrical conductivities scale with carbon concentration. Fig. 3.9 shows the behavior of these two conductivities with XPS-

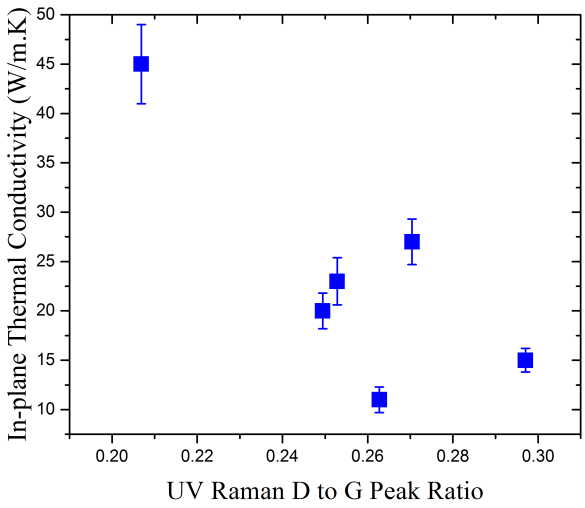

(a)

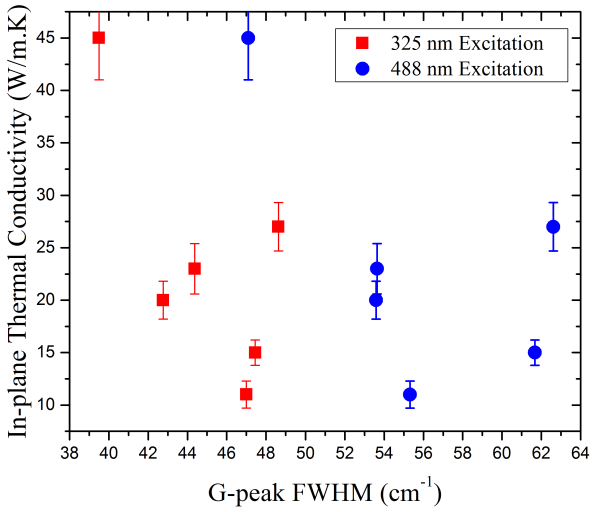

(b)

Figure 3.8: The behavior of thermal conductivity with UV and visible Raman characteristics: (a) Raman D to G peak intensity ratio and (b) Raman G peak width. Both G peak width and D to G peak intensity ratio is used as a measure of disorder, which is decreased owing to the reduction, leading to thermal conductivity to increase constantly.

extracted carbon concentration. Fig. 3.9 (a) shows the correlation of thermal conductivity to the carbon concentration plotted for this work along with our other reported values for graphene laminate and thermally annealed rGO films [1, 33]. It seems that thermal conductivity increases, with almost a quadratic trend, as the concentration of carbon atoms increases.

3.4 Theoretical analysis

In order to theoretically interpret the results, the methodology developed for thermal conductivity of graphite was used [11] to better understand the results achieved for chemically annealed rGO films. In this calculation, the phonon energy dispersion of graphite obtained within Born-von Karman model of lattice dynamics [65, 66] has been used and oxygen and other impurities have been considered as point defects. As discussed in ref [11], for phonon frequencies larger than cut-off frequency, $\omega_s > \omega_{c,s}$, a two dimensional (2D) phonon transport is assumed in rGO films and for phonon frequencies below that, $\omega_s \leq \omega_{c,s}$, phonon transport is assumed to be three dimensional (3D). Here $\omega_{c,s}$ is the low-bound cutoff frequency of the s-th phonon branch. Therefore, the in-plane thermal conductivity can be written as:

$$
\begin{aligned}
K^{in-plane} &= K^{3D} + K^{2D} \\
K^{3D} &= \frac{\hbar^2}{4\pi^2 K_B T^2} \sum_{s=LA,TA,ZA} \frac{1}{V_s^{\perp}} \int_0^{\omega_{c,s}} [\omega_s^{\parallel}(q_{\parallel})]^3 \tau(\omega_s^{\parallel}) v_s^{\parallel}(q_{\parallel}) \frac{exp(\frac{\hbar\omega_S^{\parallel}}{K_B T})}{[exp(\hbar\omega_S^{\parallel}) - 1]^2} q_{\parallel} d\omega_s^{\parallel} \\
K^{2D} &= \frac{\hbar^2}{4\pi^2 K_B T^2} \sum_{s=LA,TA,ZA} \frac{\omega_{c,s}}{V_s^{\perp}} \int_{\omega_{c,s}}^{\omega_{max,s}} [\omega_s^{\parallel}(q_{\parallel})]^2 \tau(\omega_s^{\parallel}) v_s^{\parallel}(q_{\parallel}) \frac{exp(\frac{\hbar\omega_S^{\parallel}}{K_B T})}{[exp(\hbar\omega_S^{\parallel}) - 1]^2} q_{\parallel} d\omega_s^{\parallel}
\end{aligned}
\tag{3.1}
$$

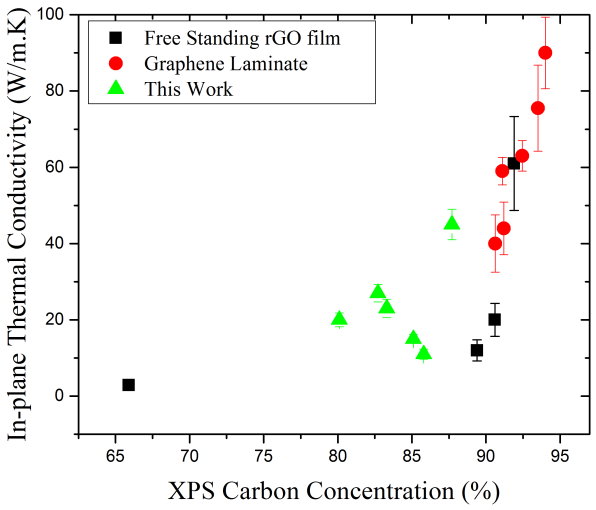

(a)

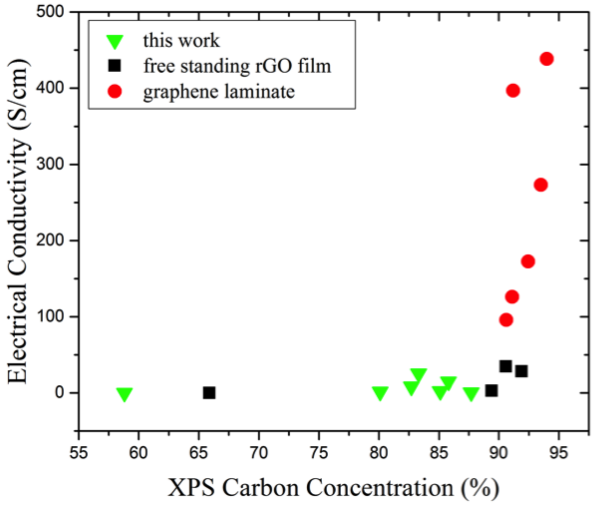

(b)

Figure 3.9: Correlation of (a) thermal and (b) electrical conductivities of rGO films with carbon concentration plotted along with other reported values for graphene laminate and thermally reduced rGO films [1, 33]. As carbon concentration exceeds ~ 90% both electrical and thermal conductivities increase significantly.

Where, $\tau_{s,\omega}$ denotes the relaxation time for a phonon with the frequency ω from the s-th acoustic phonon branch, $\overrightarrow{q}(q_{\parallel}, q_z)$ is the phonon wave vector, $v_s = d\omega/dq_{\parallel}$ is the in-plane phonon group velocity for s-th branch, T is the temperature, K_B is the Boltzmanns constant, $\hbar$ is the Planks constant. In the summation six lowest phonon branches were considered: in-plane longitudinal acoustic LA_1, in-plane transverse acoustic TA_1, out-of-plane transverse acoustic ZA, in-plane longitudinal acoustic-like LA_2, in-plane transverse acoustic-like TA_2 and out-of-plane transverse acoustic-like ZO'.

The total phonon relaxation time can be written as the sum of three components assuming that thermal conductivity is limited by three main scattering mechanism: Umklapp scattering (U), point-defect scattering (PD) and scattering on ordered clusters edges (E). Therefore, using the Matthiessens rule as [11, 13, 14, 67–69]: $1/\tau = 1/\tau_{pd,s} + 1/\tau_{U,s} + 1/\tau_{E,s}$, the total phonon relaxation time is calculated, where $\tau_{E,s}(\omega) = L/v_s^{\parallel}$, $\tau_{U,s}(\omega) = M{v_s}^2\omega_{max,s}/(\gamma_s^2 K_B T[\omega]^2)$ and $\tau_{PD,s}(\omega) = 4v_s^{\parallel}/(s_0\Gamma q^{\parallel}\omega^2)$. Here γ denotes the average Gruneisen parameter which depends on the phonon branch and is equal to: $\gamma_{LA_1,LA_2} = 2$, $\gamma_{TA_1,TA_2} = 1$, $\gamma_{ZA,ZO'} = -1.5$. $\omega_{max,s}$ is the maximum frequency of s-th phonon branch, s_0 is the cross-section area per atom, M is the graphite unit cell mass, Γ is the measure of the strength of the point-defect scattering due to mass-difference and L is the average length of ordered sp^2 or sp^3 clusters.

The value of cut-off frequency of the s-th phonon branch is determined from the phonon spectra as the highest energy of s-th branch along c-axis direction:$\omega_{c,LA_1/LA_2} = 89cm^{-1}$, $\omega_{c,TA_1/TA_2} = 89cm^{-1}$, $\omega_{c,ZA/ZO'} = 32cm^{-1}$ and finally Γ determines the strength of point-defects scattering and is estimated by [67]: $\Gamma = \sum_i c_i(\Delta M_i/M_C)^2$, where $\Delta M_i =$

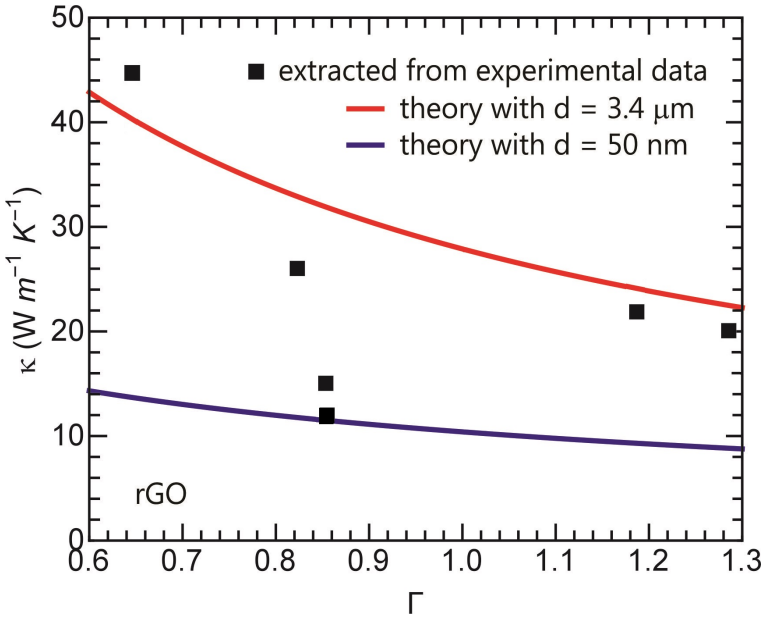

Figure 3.10: The calculation results of the in-plane thermal conductivity of reduced GO film at RT as a function of parameter plotted for two different graphitic cluster size d= 50 nm and d= 3.4 . The calculation results have been plotted along with experimental results for comparison.

$M_{d,i} - M_C$ is the difference between the mass of point-defects $M_{d,i}$ and the mass of carbon atom M_C, and c_i is the ratio between the concentrations of the defects i and carbon atoms. As stated before, any atom other than carbon was considered as impurities attached to carbon showing their effect as a point-defects in graphite lattice. The parameter has been calculated for each atom using XPS extracted atomic concentrations and is shown in Table 3.2. As it is depicted in Fig. 3.9 (a), there are two data points (shown in green triangles) which their thermal conductivities decrease as the concentration of carbon atoms increases. The two data points belong to sample HI-2 and HI-300-2. This behavior is explained by the fact that thermal conductivity is not only a function of point-defects concentration but also depends on the average graphene cluster size. Fig. 3.10 Shows the results of calculations for

the dependence of in-plane thermal conductivity of rGO films as a function of Γ parameter depicted for two different L values, where L is the average length of the ordered graphitic clusters. The calculation results have been plotted along with experimental data points. Here is how the experimental results are interpreted: as a result of reduction, oxygen atoms are released from the film leading to the concentration of oxygen atoms to decrease and thus concentration of carbon atoms to increase constantly. This is modeled in our calculation using Γ parameter, which is determined from the concentration and mass of point defects (oxygen and other impurities). Generally, as the concentration of carbon atoms increases, the total concentration of point defects decreases leading to the Γ parameter to decrease. However, since Γ also depends on the mass density of point defects, this trend can be affected based on the atomic mass of impurities. The same behavior was observed for the thermally reduced rGO samples [33].

Thermal conductivity seems to have more intriguing behavior with Γ parameter (See Fig. 3.10) since the average cluster size of graphitic regions would come into account. Having the in-plane thermal conductivity and Γ parameter from experiment, the average length of graphitic clusters can be extracted from theoretical results (see Fig. 3.10). These results can be used to explain the lower thermal conductivity values observed for sample HI-2 and HI-300-2 despite their higher carbon concentration, which is attributed to their lower graphitic clustering size. Electrical conductivity also shows the same increasing behavior as the carbon concentration is increased (See Fig. 3.9 (b)). The study is important for the use of rGO in thermal management applications.

Chapter 4

Thermal conductivity of graphene with defects

Graphene [1] [32] has exceptionally high intrinsic thermal conductivity [7, 10]. The measurements of thermal conductivity of large suspended graphene samples using the optothermal Raman technique revealed thermal conductivity values exceeding those of bulk graphite, which has thermal conductivity of ~ 2000 W/mK at room temperature (RT) [10]. Independent measurements with the optothermal Raman technique [24, 70] and the scanning thermal microscopy [71] confirmed the excellent heat conduction properties of graphene. Theoretical considerations suggest that graphene can have higher thermal conductivity than that of the graphite basal planes despite similar phonon dispersions and crystal lattice anharmonicities. This fact is attributed to an unusually long mean free path (MFP) of the

[1] This section of dissertation follows the published material from H. Malekpour, P. Ramnani, S. Srinivasan, G. Balasubramanian, D. L. Nika, A. Mulchandani, R. K. Lake, A. A. Balandin, *Nanoscale* **8**, 14608 (2016)

long-wavelength phonons in two-dimensional (2D) lattices [10, 19, 23]. Recent calculations by different methods suggested that the graphene sample size should be in the 100 μm [11, 21] or even 1 mm [22] range in order to fully recover the intrinsic thermal conductivity limited only by the lattice anharmonicity, i.e. without phonon scattering by defects, polycrystalline grains, and edges of the samples. The intrinsic thermal conductivity values obtained in these works ranged from 4000-6000 W/mK near RT [11, 21, 22]. In other terms, the high intrinsic thermal conductivity of graphene can be explained by the fact that the phonon Umklapp scattering is less efficient in restoring thermal equilibrium in 2D systems than in bulk three-dimensional (3D) systems [11, 14, 72].

The thermal conductivity of graphene can be degraded by defects such as polymer residue from nanofabrication [73], edge roughness [19], polycrystalline grain boundaries [74], and disorder from contact with a substrate or a capping layer [25, 75, 76]. For this reason, the thermal conductivity of graphene synthesized by the chemical vapor deposition (CVD) is always lower than that of the mechanically exfoliated graphene from highly ordered pyrolytic graphite (HOPG) [7, 24, 34–36]. A possible loss of polycrystalline grain orientation in the average quality CVD graphene can lead to additional degradation of the thermal conductivity [77]. However, to date, there have been no quantitative experimental studies of the thermal conductivity dependence on the concentration of defects, N_D, in graphene. The only reported experimental study of the phonon-point-defect scattering in graphene utilized isotopically modified graphene [78]. The phonon scattering on isotope impurities is limited to the mass-difference term only. It does not include the local strain effects owing to missing atoms, bond breaking or presence of chemical impurities. It was established in

Ref. [78] that the dependence of the thermal conductivity on the isotope impurity (^{13}C) concentration is in line with the prediction of the well-established virtual crystal model [79] used to calculate thermal conductivity in alloy semiconductors such as Si_xGe_{1-x} [79] or $Al_xGa_{1-x}As$ [80]. This model predicts the highest K for the material with either x=0 or (1-x)=0 and a fast decrease to a minimum as x deviates from 0. The situation is expected to be different in materials with defects induced by irradiation.

The knowledge of the K dependence on the concentration of defects induced by irradiation can shed light on the strength of the phonon-point defect scattering in 2D materials. The change in the dimensionality results in different dependencies of the scattering rates on the phonon wavelengths in the processes of phonon relaxation by defects and grain boundaries [13, 19, 67]. In bulk 3D crystals, the phonon scattering rate on point defects, $1/\tau_P$, varies as $\sim 1/f^4$ (where f is the phonon frequency) [67]. Owing to the changed phonon density of states (PDOS), the phonon scattering rate in 2D graphene has a different frequency dependence, $1/\tau_P \sim 1/f^3$, which can, in principle, affect the phonon MFP and the thermal conductivity. In addition to the fundamental scientific interest, a quantitative study of the dependence of thermal conductivity on density of defects is important for practical applications of graphene in thermal management. The graphene and few-layer graphene (FLG) heat spreaders [29, 81, 82] will likely be produced by CVD while FLG thermal fillers in thermal interface materials (TIMs) [26, 83, 84] will be synthesized via the liquid phase exfoliation (LPE) technique. Both methods typically provide graphene with a large density of defects than that exfoliated from HOPG. Here in this study I report the results of an investigation of the thermal conductivity of suspended CVD grown single layer graphene

(SLG) as a function of the density of defects, N_D. the details of this experiment is discussed in the following sections.

4.1 Preparing the experimental set up

In order to study the effect of defects on thermal conductivity of graphene, chemical vapor deposition (CVD) technique was used to grow single layer graphene. The single layer graphene samples were fabricated using ambient pressure chemical vapor deposition (AP-CVD) on a Cu foil [85]. Briefly, a polycrystalline Cu foil (99.8%, Alfa Aesar) was cleaned in acetic acid, acetone and IPA to remove any surface oxides. The cleaned Cu foil was loaded into the CVD chamber and the furnace temperature was ramped to $1030°C$ while flowing Ar and H_2 and the foil was annealed for 2 hours. For the growth of graphene, methane (90 ppm) along with Ar and H2 was introduced into the chamber for 20 minutes. After growth, the furnace was turned off and cooled to room temperature in Ar and H_2 atmosphere. Then, the SLG grains were transferred on to a metallic (gold) TEM grid using a direct transfer method to avoid any contamination from the polymer support layer. Briefly, a TEM grid (G2000, 7.5 μm square holes, TedPella) was placed directly on the Cu foil/graphene stack along with a drop of isopropyl alcohol (IPA). On heating, as the IPA evaporates the surface tension draws the graphene and metallic grid together into intimate contact. The Cu foil is then etched in ferric chloride, washed in DI water and the resulting graphene on TEM grid is dried and used for subsequent Raman measurements. The gold TEM grid with the thickness of 25 microns acts as a heat sink in our experimental set up. The CVD-grown single layer graphene is suspended over square holes of 7.5 microns on TEM grid. The

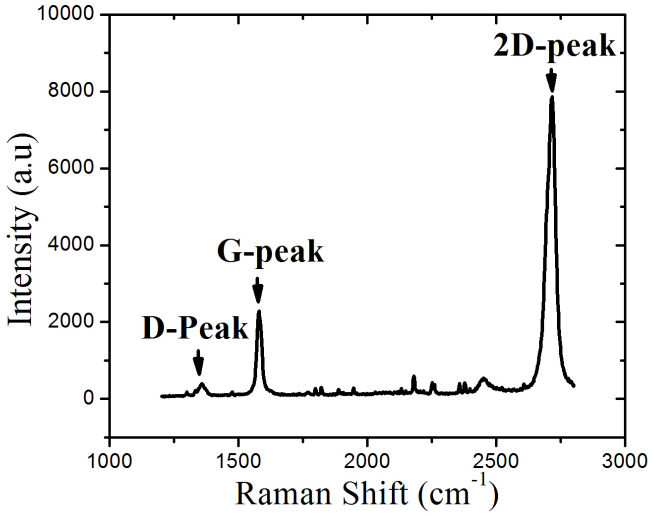

Figure 4.1: Raman Spectrum of the suspended CVD grown SLG. A small D peak appears even before any irradiation step is applied which is a characteristic of CVD grown graphene. The figure is reproduced from H. Malekpour, P. Ramnani, S. Srinivasan, G. Balasubramanian, D. L. Nika, A. Mulchandani, R. K. Lake, A. A. Balandin, *Nanoscale* **8**, 14608 (2016) with permission from Royal Society of Chemistry.

quality of transferred graphene is studied using Raman spectroscopy. Fig. 4.1 depicts the Raman spectrum of CVD-grown graphene before any irradiation step is applied. One should note that even before irradiation a small D-peak appears in the Raman spectrum, showing the presence of defects, which is a characteristic of CVD-grown graphene. Scanning Electron Microscopy (SEM) is used to locate suspended graphene areas, fully covering a hole on TEM grid. Fig. 4.2 shows an SEM image of the sample with partially and fully covered areas of suspended graphene. Three different fully covered SLG spots were chosen for our thermal studies, referred to as SLG # 1, SLG # 2 and SLG # 3, in the rest of this chapter.

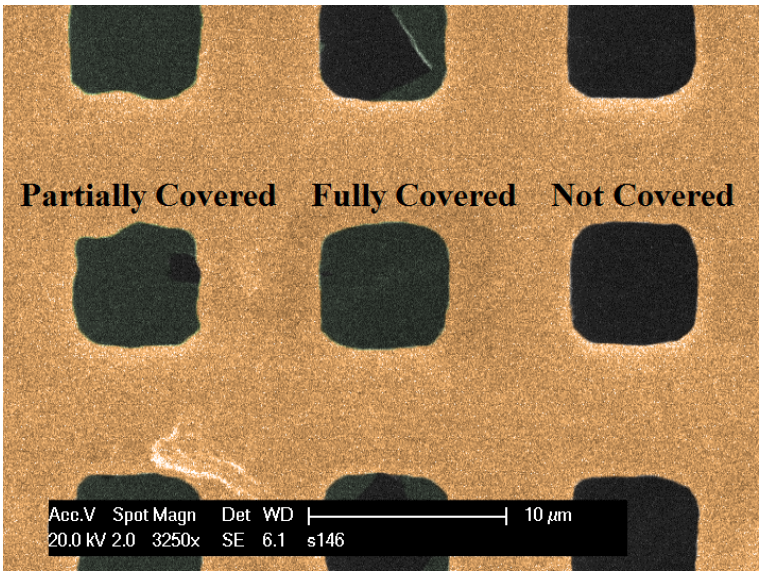

Figure 4.2: Scanning electron microscopy image of graphene transferred on gold TEM grid showing 7.5 m array of square holes. Some holes are fully or partially covered with the graphene flake. The grid is depicted in gold color, the holes are shown in black and the almost transparent greenish areas are suspended graphene flakes. The figure is reproduced from H. Malekpour, P. Ramnani, S. Srinivasan, G. Balasubramanian, D. L. Nika, A. Mulchandani, R. K. Lake, A. A. Balandin, *Nanoscale* **8**, 14608 (2016) with permission from Royal Society of Chemistry.

4.2 Introducing defects using low energy electron beam irradiation

The suspended SLG areas were exposed to 20 KeV electron beam to induce defects in Graphene in a controllable way for our thermal studies [86, 87]. Philips XL-30 FEG field-emission system was used for this purpose. The irradiation process was done inside vacuum chamber with the pressure set to be below 10^{-4} $Torr$. The suspended graphene areas were exposed to continuous electron beam from electron gun with current varying from ~ 3 nA to ~ $10nA$ controlled by the beam spot size. In order to set the beam current, Faraday cup was used to read the beam current at desired spot size before each step of irradiation. A constant magnification was maintained during all irradiation steps in to keep the irradiated area constant, therefore the dose density rate is controlled by irradiation time. After each step of irradiation, Raman spectroscopy was used to quantify the amount of induced defects. Fig. 4.3 depicts the evolution of Raman spectrum after four steps of irradiation. As the sample undergoes more steps of irradiation, the Raman D peak intensity ratio increase leading to Raman D to G peak intensity ratio, , I_D/I_G, increases from 0.13 for as-grown CVD graphene all the way to 1.00, after four steps of the electron beam irradiation (Fig. 4.3).The presence of D-peak in the spectrum before irradiation indicates a background defects concentration characteristic for CVD graphene and explains K-value somewhat below graphite bulk limit [10, 88]. The Raman D to G peak intensity ratio is later used to quantify the amount of induced defects, which is going to be discussed in next section.

4.3 Quantifying defects using Raman spectroscopy

The evolution of the Raman spectrum under irradiation was used for quantifying the density of defects, N_D, following a conventional formula [60, 89]:

$$N_D(cm^{-2}) = \frac{(1.8 \pm 0.5) \times 10^{22}}{\lambda^4}(\frac{I_D}{I_G}) \tag{4.1}$$

Where λ is the excitation wavelength and N_D is the density of defects. It is known that Eq. 4.1 is valid for a relatively low defect-density regime. The criterion was met in these experiments. The density of defects increases linearly with the Raman D to G peak intensity ratio. To investigate the correlation between the density of defects and the e-beam irradiation dose, the Raman D to G peak intensity ratio, I_D/I_G, is plotted as a function of the total irradiation dose in Fig. 4.4. The Raman D to G peak intensity ratio increases linearly with irradiation dose, which is compatible with previous reports for the low defect-density regime [86].

4.4 Investigating nature of defects

In addition to the quantity of defects, the origin of defects can be investigated using Raman spectroscopy. It is reported that the nature of defects correlates with Raman D to D' peak intensity ratio [90]. It has been shown that $I(D)/I(D')$ in graphene attains its maximum ($\simeq$ 13) for the defects associated with sp^3 hybridization, decreases for the vacancy-like defects ($\simeq$ 7) and reaches a minimum for the boundary-like defects ($\simeq$ 3.5) [91]. Following this approach the nature of defects was found to be vacancies. For this investigation, the

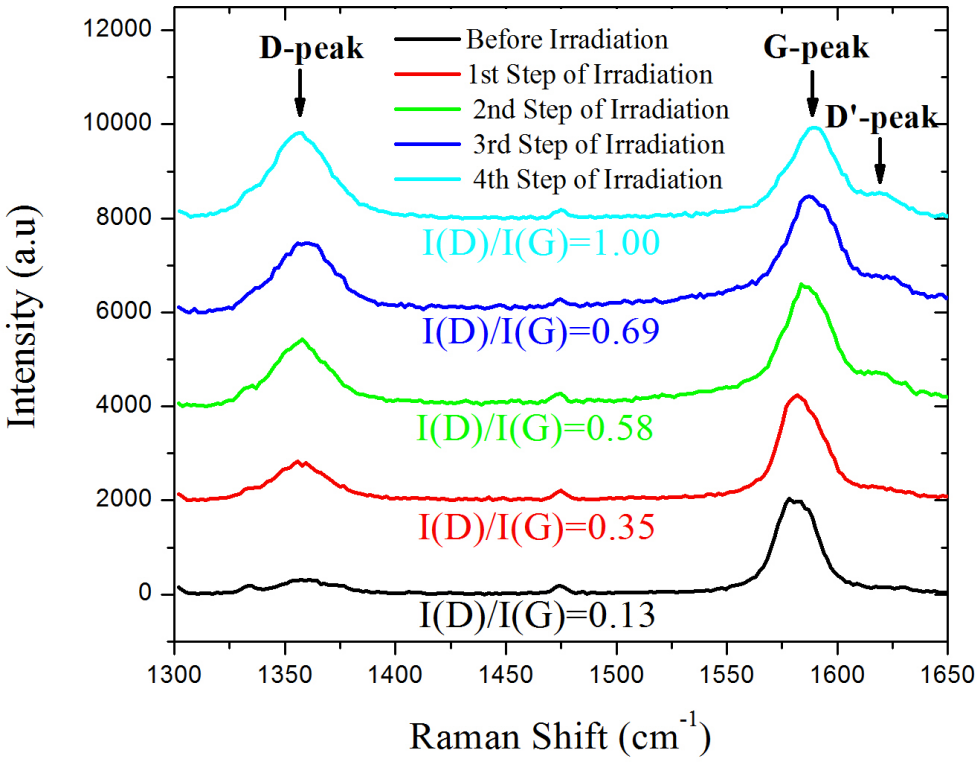

Figure 4.3: Evolution of Raman spectrum under electron beam irradiation. As the sample is exposed to the electron beam, the Raman D peak intensity increases resulting in a D-to-G peak intensity ratio change from ~ 0.13 to ~ 1.00. The Raman G peak shifts to higher frequencies and the D' peak appears at ~ 1620 cm^1. The Raman D to G peak intensity ratio is used to quantify the amount of induced defects. The figure is reproduced from H. Malekpour, P. Ramnani, S. Srinivasan, G. Balasubramanian, D. L. Nika, A. Mulchandani, R. K. Lake, A. A. Balandin, *Nanoscale* **8**, 14608 (2016) with permission from Royal Society of Chemistry.

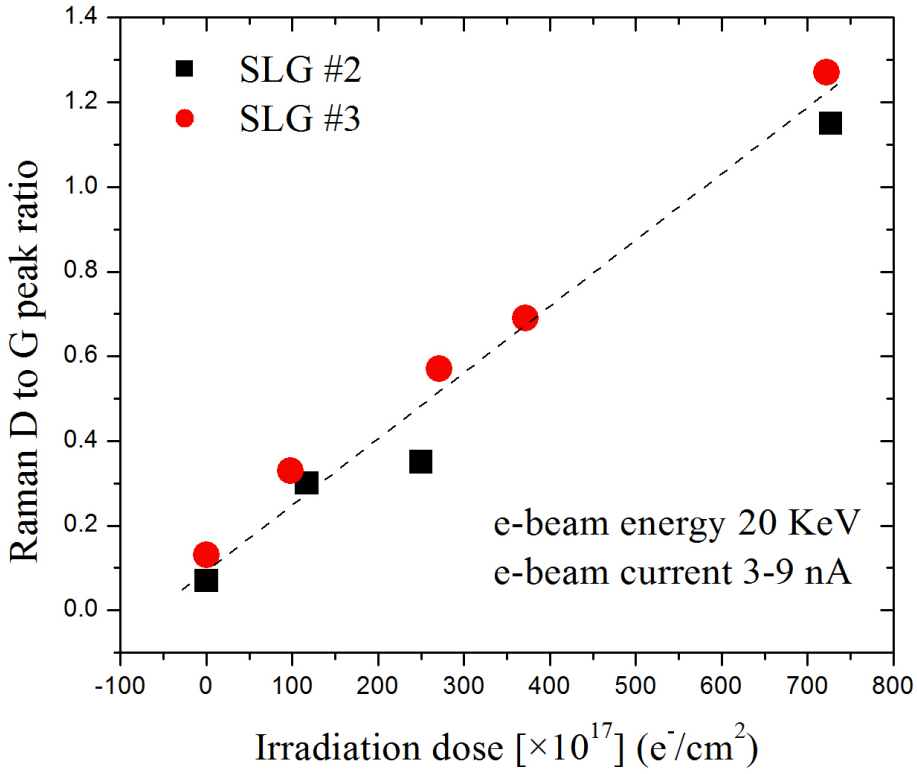

Figure 4.4: Correlation of the Raman D-to-G peak intensity ratio with the electron beam irradiation dose. The low energy 20 keV electron beam was used to irradiate graphene. The beam current varied from ~ 3 to ~ 9 nA. The Raman D-to-G peak intensity ratio depends linearly on the irradiation dose. The figure is reproduced from H. Malekpour, P. Ramnani, S. Srinivasan, G. Balasubramanian, D. L. Nika, A. Mulchandani, R. K. Lake, A. A. Balandin, *Nanoscale* **8**, 14608 (2016) with permission from Royal Society of Chemistry.

Raman D and G peaks are fitted with Lorentzian functions and the D' peak by a Fano line shape. Fig. 4.5 shows the detail of the Raman curve fitting. The intensity Ratio of Raman D to G peaks is plotted as a function of Raman D' to G peaks intensity ratio (see Fig. 4.6) and it was found that the slop of this plot, which shows $I(D)/I(D')$, is constant and equal to ~ 7, attributed to vacancy type defect [91]. It is known that the intensity of D band depends not only on the concentration of defects [90], but also on the type of defects and only defects that are capable of scattering electrons between the two valleys K and K' of Brillouin zone can contribute to the D band [92–94]. For this reason not all types of defects in graphene can be detected by Raman spectroscopy.

4.5 Thermal conductivity of graphene and e-beam irradiated graphene

In this study [2], OTR technique was used for investigating thermal properties of graphene samples. As it was discussed chapter 1, in optothermal Raman technique, which is a non-contact steady-state technique, the micro-Raman spectrometer acts both as a heater and thermometer and the sample is suspended over a heat sink which in our case is a gold TEM grid. The measurement is done in two steps: the calibration measurement and the power-dependent Raman measurement. For calibration measurement, a low-power excitation laser is used to record the Raman spectra of graphene sample in a wide temperature range [7]. For this purpose, the sample is placed inside a cold-hot cell (Linkam 600), where the temperature is controlled externally with the steps of $10°C$ and accuracy of $0.1°C$. To

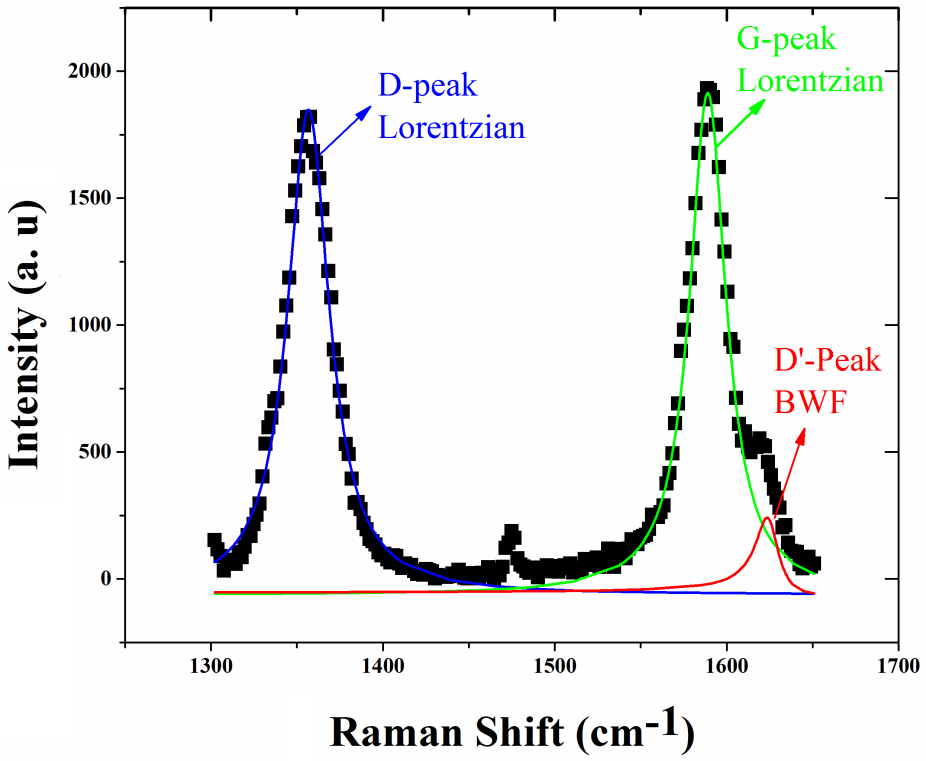

Figure 4.5: The detail of Raman curve fitting performed in order to investigate nature of defects: Raman D and G peaks are fitted with Lorentzian functions and the D' peak by a Fano line shape. The figure is reproduced from H. Malekpour, P. Ramnani, S. Srinivasan, G. Balasubramanian, D. L. Nika, A. Mulchandani, R. K. Lake, A. A. Balandin, *Nanoscale* **8**, 14608 (2016) with permission from Royal Society of Chemistry.

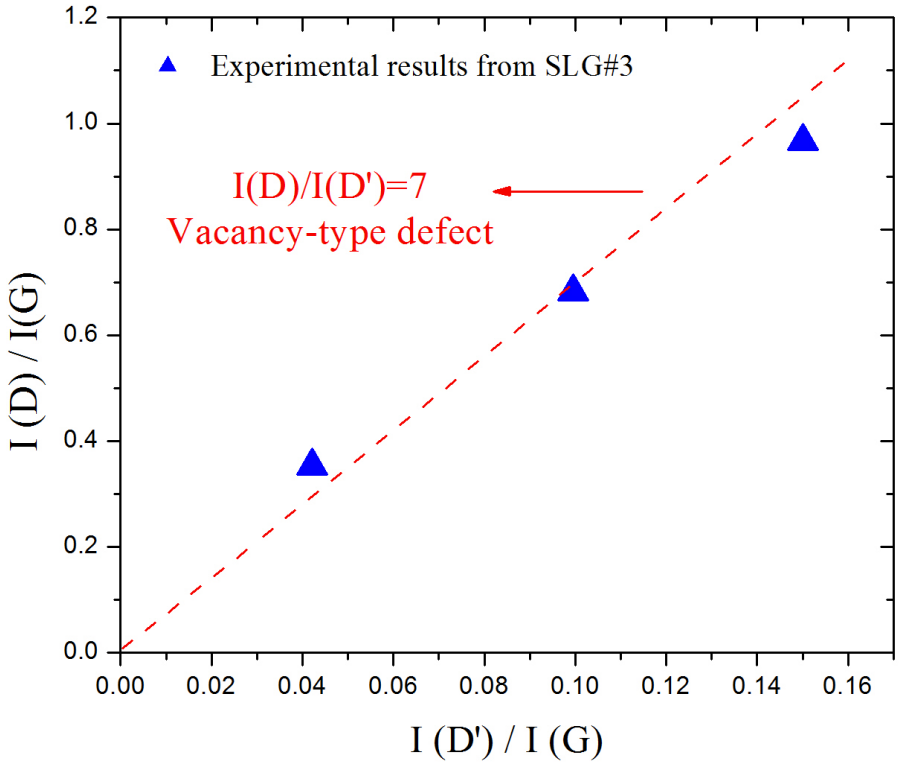

Figure 4.6: Nature of defects has been found to be mostly vacancies based their Raman spectrum analysis. The Raman D to D' peak intensity ratio of ~ 7 has been achieved, for SLG 3 at different steps of irradiations, which has been attributed to vacancy type defect [91]. The figure is reproduced from H. Malekpour, P. Ramnani, S. Srinivasan, G. Balasubramanian, D. L. Nika, A. Mulchandani, R. K. Lake, A. A. Balandin, *Nanoscale* **8**, 14608 (2016) with permission from Royal Society of Chemistry.

stabilize the temperature, the samples were kept at each temperature step for around 5 minutes and then Raman G peak positions were recorded. Low laser excitation power of $\sim 0.5\ mW$ was used in our experiments to avoid any local heating caused by the laser which could affect the local temperature. As a result of calibration measurement, the position of the Raman G peak is determined as a function of the sample temperature. In the second step of the optothermal measurements, the Raman spectrum of sample is recorded as a function of increasing excitation power.

For this purpose, the excitation laser power is intentionally increased to cause the local heating of the suspended graphene. The spectral position of the Raman G peak indicates the local temperature rise in response to the laser heating with the help of the calibration characteristic. Having these two measurements done, one can extract thermal conductivity of the sample [7].

Fig. 4.7 demonstrates the experimental results of calibration (a) and power measurement (b) measurement for SLG before any irradiation step is applied. As depicted in Fig. 4.7 (a) the Raman G peak spectral position depends linearly on the sample temperature in the examined temperature interval and the extracted temperature coefficient $\chi_G = 0.013\ cm^{-1}/^{\circ}C$ which is in line with previous reported values for graphene [63]. The shift of Raman G-peak with increasing laser power is plotted in Fig. 4.7 (b). An excellent linear drop of G peak position is clearly seen in this figure. One of the important factors that needs to be measured is the absorption coefficient of suspended graphene sample. It is known that the absorption of graphene depends on the excitation wavelength and numerical aperture of the objective lens. However in practical too many factors can affect this

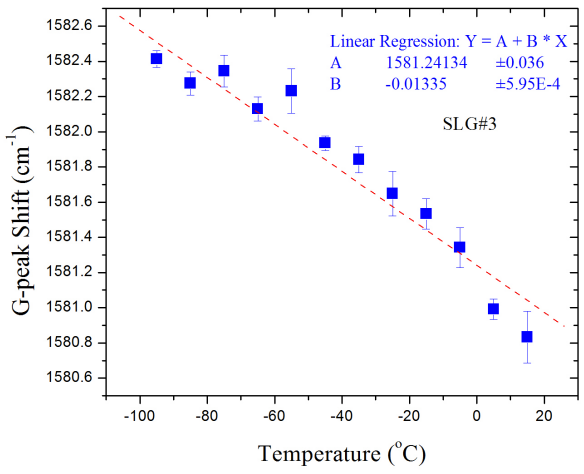

(a)

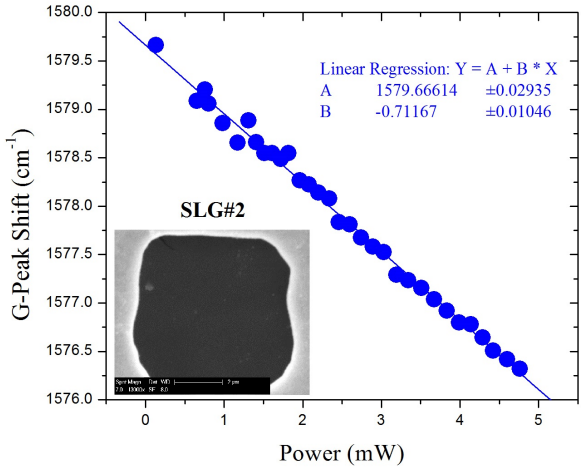

(b)

Figure 4.7: Raman spectroscopy data for extraction of thermal conductivity of suspended CVD graphene flakes. (a) Calibration dependence of the Raman G peak position as a function of temperature. The measurement was conducted before graphene exposure to the electron beam. (b) Raman G peak position dependence on the power on the excitation laser. The SEM image of this sample is depicted in the inset. The results demonstrate an excellent linear trend. The figure is reproduced from H. Malekpour, P. Ramnani, S. Srinivasan, G. Balasubramanian, D. L. Nika, A. Mulchandani, R. K. Lake, A. A. Balandin, *Nanoscale* **8**, 14608 (2016) with permission from Royal Society of Chemistry.

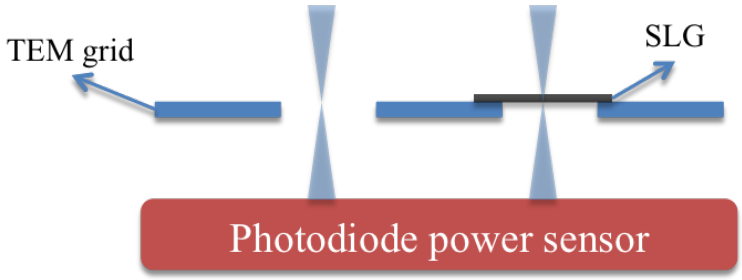

Figure 4.8: Schematic of the direct procedure for direct measurement of absorption coefficient for SLG.

absorption such as surface contamination, defects and bending [10, 95–97]. Therefore, the experimental absorption coefficient was measured directly by placing a photodiode power meter (Ophir) under the sample (Fig. 4.8). The portion of light absorbed by suspended graphene, which causes the local heating, was measured for a graphene covered hole and a reference empty hole. The difference in power reading corresponds to the power absorbed by graphene at a given laser wavelength. The measurement was repeated ten times at different laser power levels to dteremine the absorption coefficient of $5.68\% \pm 0.72\%$ at the excitation laser wavelength of $\lambda = 488\ nm$

The slope of the power-dependent Raman measurement, $w_G(PD)$ line in Fig. 4.7 (b), carries information about the value of thermal conductivity K. To extract thermal conductivity value, heat diffusion equation was solved, for the specific sample geometry. COMSOL software package in two dimensions (2D) was used for numerical solution of the equation with proper boundary conditions following the procedure explained in chapter 1. Fig. 4.9 shows the simulation results and how thermal conductivity is extracted having θ from experiment. The thermal conductivity of suspended CVD graphene was found to be around 1800 W/mK near room temperature (RT), before introduction of defects. This

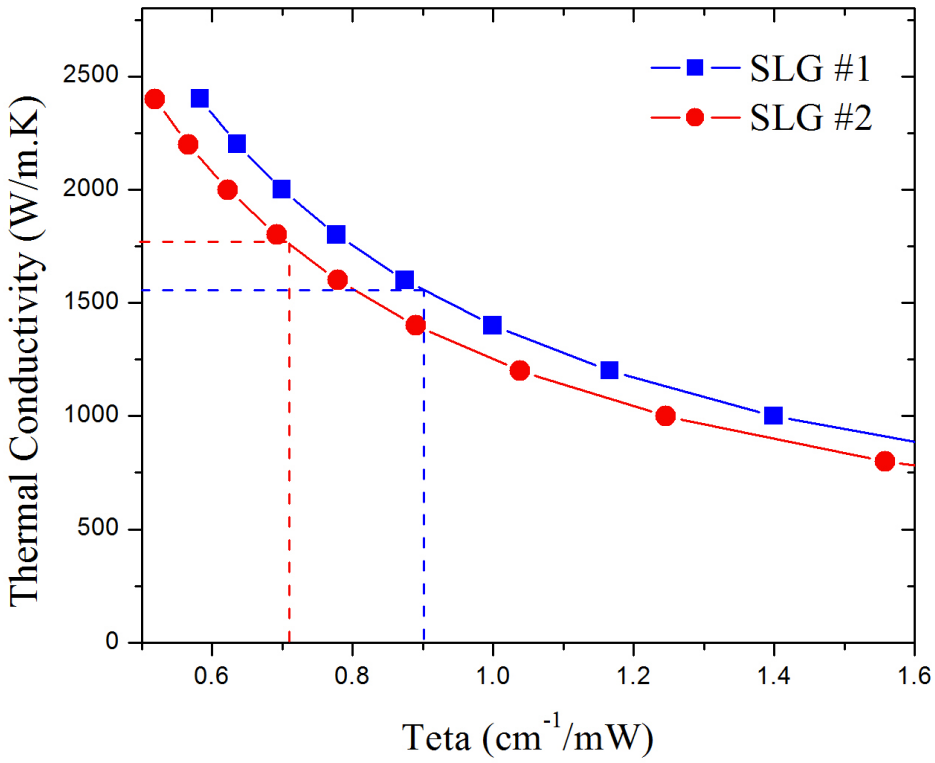

Figure 4.9: Typical simulation results obtained from the COMSOL modeling showing the θ factor. Thermal conductivity can be directly extracted having power-dependent Raman measurement slope. The figure is reproduced from H. Malekpour, P. Ramnani, S. Srinivasan, G. Balasubramanian, D. L. Nika, A. Mulchandani, R. K. Lake, A. A. Balandin, *Nanoscale* **8**, 14608 (2016) with permission from Royal Society of Chemistry.

value is in line with the previous reported values for CVD graphene [24, 70]. This value is smaller than that of graphene obtained by mechanical exfoliation from the highly oriented pyrolytic graphite (HOPG) due to the possible presence of few grain boundaries and defects introduced during synthesis and transfer, which all reduce the thermal conductivity of CVD graphene [7, 10, 35, 36]. Following the same approach thermal conductivity was obtained after each step of irradiation. It was found that the calibration measurement results remain

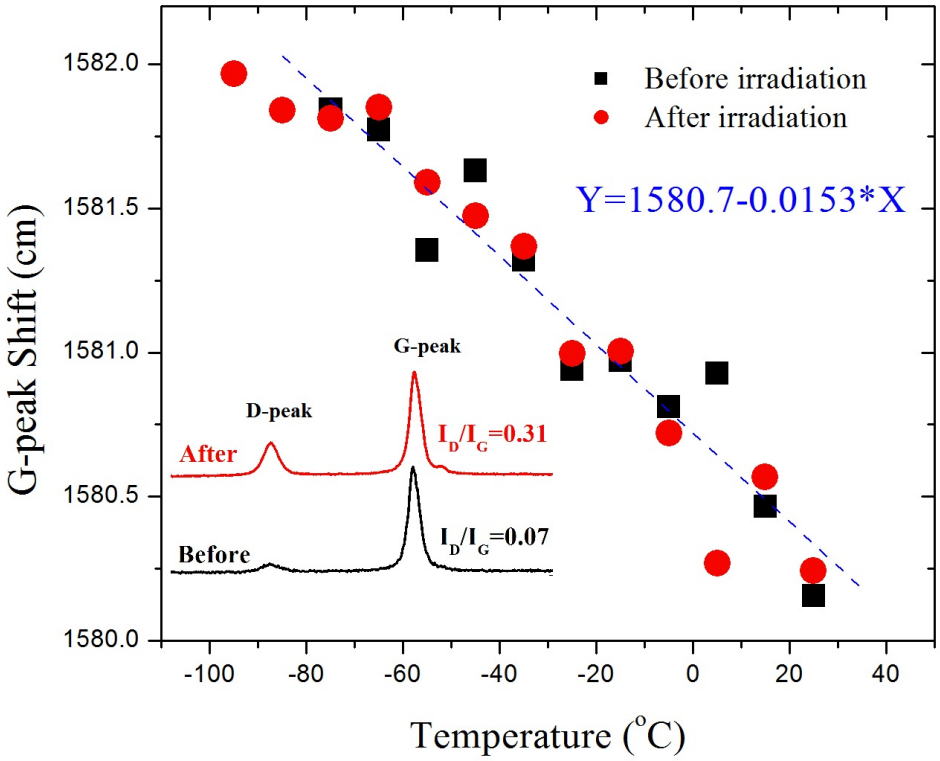

Figure 4.10: Calibration measurement done on SLG 2 before and after the irradiation procedure. The temperature coefficient of the Raman G-peak are not affected by irradiation and can be assumed constant. The figure is reproduced from H. Malekpour, P. Ramnani, S. Srinivasan, G. Balasubramanian, D. L. Nika, A. Mulchandani, R. K. Lake, A. A. Balandin, *Nanoscale* **8**, 14608 (2016) with permission from Royal Society of Chemistry.

almost the same after irradiation is applied (see Fig. 4.10).

For simplicity, the calibration measurement was done once for each spot and was assumed constant after irradiation is applied. One of the challenging parts of the experiment was the power-dependent Raman measurement for highly irradiated samples. As the laser power was increased for power-dependent Raman measurement, local healing of induced defects occurred at the laser hot spot, leading to the Raman D to G peak intensity ratio

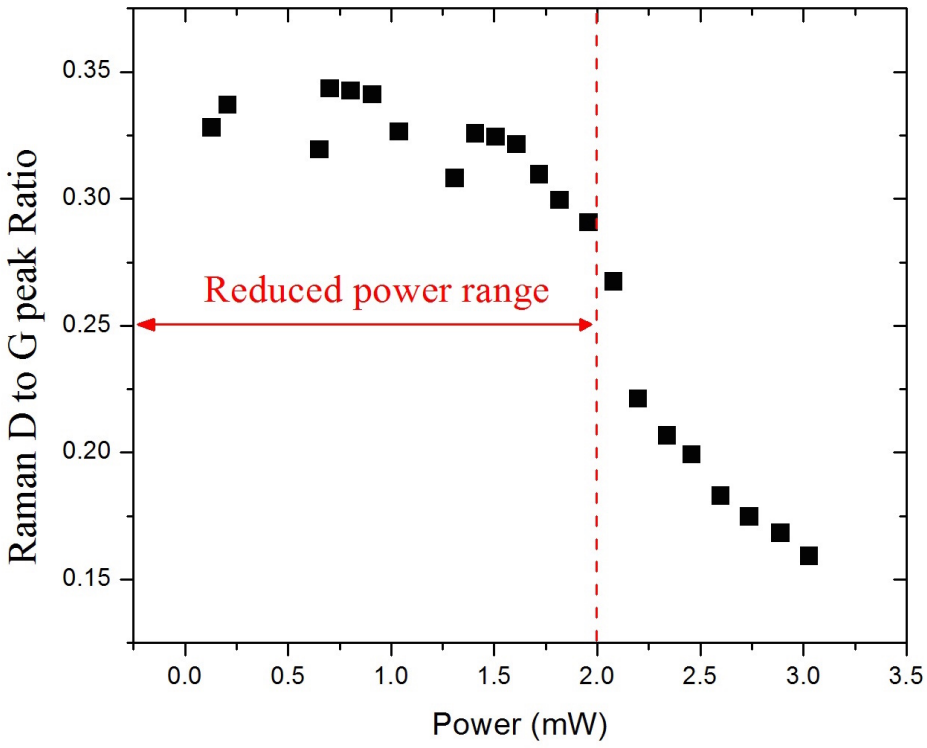

Figure 4.11: Raman D to G peak intensity ratio monitoring, during power-dependent Raman measurement, for keeping the power below critical point, at which defects starts to locally heal, used for highly irradiated samples. The figure is reproduced from H. Malekpour, P. Ramnani, S. Srinivasan, G. Balasubramanian, D. L. Nika, A. Mulchandani, R. K. Lake, A. A. Balandin, *Nanoscale* **8**, 14608 (2016) with permission from Royal Society of Chemistry.

to reduce . This is explained by the drop of thermal conductivity at high level of induced defects, which leads to the laser hot spot to reach very high temperatures at even low levels of excitation power. To solve this problem, Raman D to G peak intensity ratio was recorded during power-dependent Raman measurement of irradiated samples and the power level was kept below the critical point in which the drop of Raman D to G peak intensity ratio occurs. Fig. 4.11 depicts the details of this procedure.

Fig. 4.12 depicts the result of power-dependent Raman measurement for two levels of irradiation for the spot 3. A clear increase in the slope was measured for higher levels of irradiation indicating the decrease of thermal conductivity. The decrease in thermal conductivity means higher levels of local heating is caused by the same laser power and therefore larger shift in Raman G peak occurs.

4.6 The behavior of thermal conductivity with defects density

In Fig. 4.13 we present the extracted thermal conductivity, K, as a function of the defect density, N_D, by square, circle and triangle points corresponding to three suspended flakes of graphene. For the small defect densities, $N_D < 1.2 \times 10^{11} cm^{-2}$, the thermal conductivity decreased with increasing N_D. It can be approximated with the linear dependence $K = 1990 - 116 \times N_D$ [W/mK]. In the $N_D = 0$ limit, the thermal conductivity K=1990 W/mK was still slightly smaller than that of the ideal basal plane of HOPG due to the background defects and possible grain boundaries present in CVD graphene before irradiation. At the defect density of $N_D \sim 1.5 \times 10^{11} cm^{-2}$, one can see an intriguing change in the $K(N_D)$ slope. It can be interpreted as a strong reduction in the rate of the decrease of K with increasing concentration N_D or the on-set of saturation. The thermal conductivity in this region is still rather high $K \sim 400$ W/mK. This is clearly above the amorphous carbon limit [10]. For theoretical interpretation of the measured behavior of the thermal conductivity we employed both a BTE analysis and MD simulations.

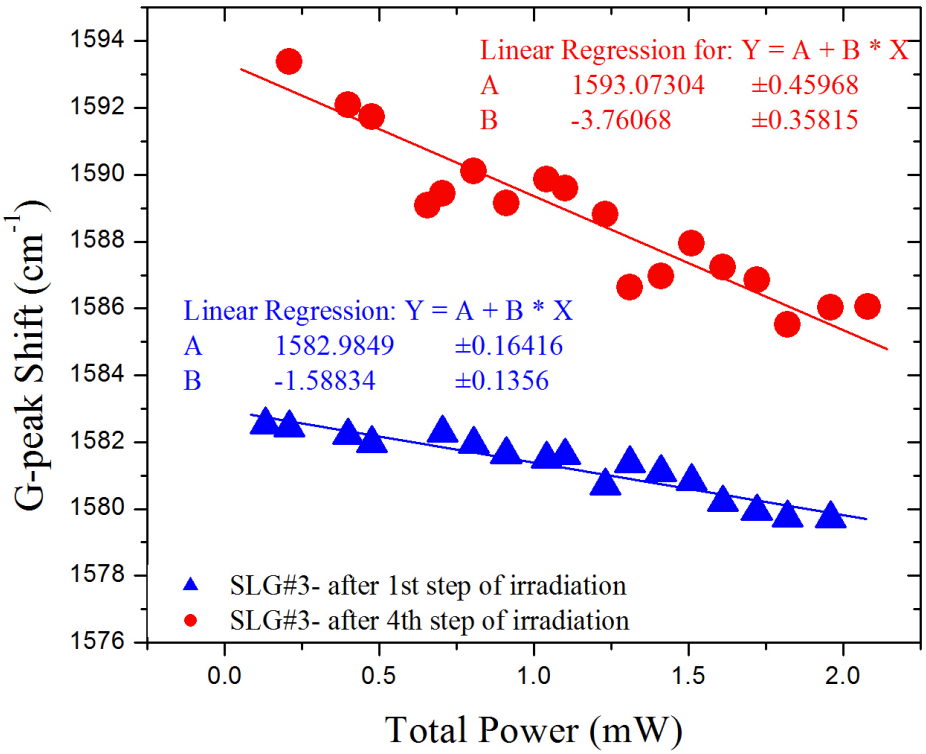

Figure 4.12: Power-dependent Raman measurement results shown for SLG 3 after the 1st and 4th steps of irradiation were applied. One should notice the increase of the slope factor, which is directly related to the suppression of thermal conductivity. The power range has been kept below 2 mW to avoid local healing of induced defects. The figure is reproduced from H. Malekpour, P. Ramnani, S. Srinivasan, G. Balasubramanian, D. L. Nika, A. Mulchandani, R. K. Lake, A. A. Balandin, *Nanoscale* **8**, 14608 (2016) with permission from Royal Society of Chemistry.

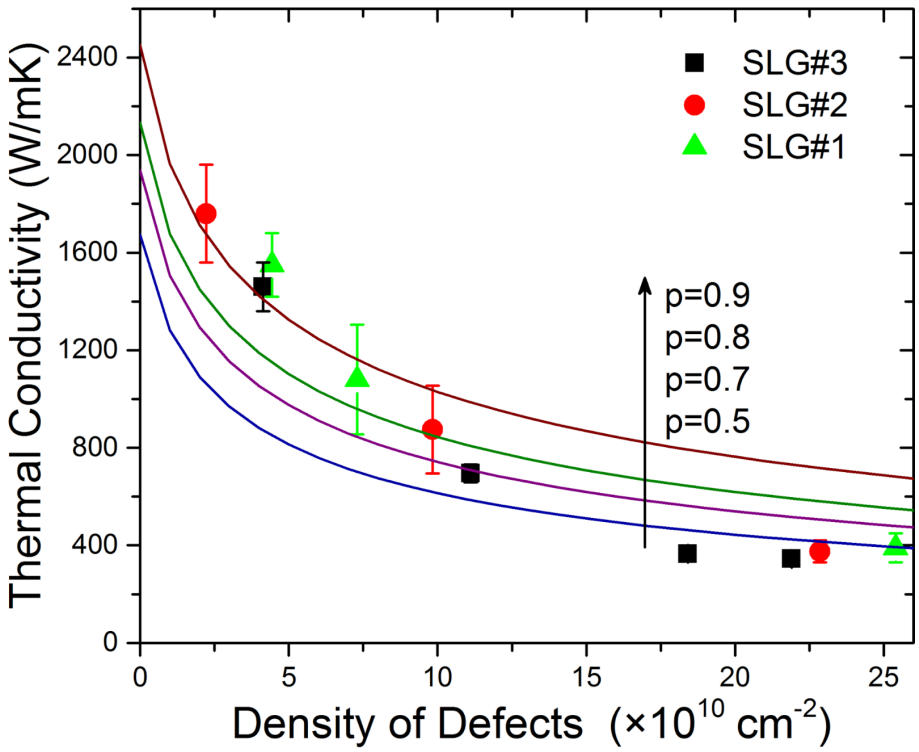

Figure 4.13: Dependence of the thermal conductivity on the density of defects. The experimental data are shown by squares, circles and triangles. The solid curves are calculated using the BTE with different values of the specularity parameter p. Note that the interplay of three phonon relaxation mechanisms-Umklapp, point-defect, and rough edge scattering-gives a thermal conductivity dependence on the defect density close to the experimentally observed trend. The figure is reproduced from H. Malekpour, P. Ramnani, S. Srinivasan, G. Balasubramanian, D. L. Nika, A. Mulchandani, R. K. Lake, A. A. Balandin, *Nanoscale* **8**, 14608 (2016) with permission from Royal Society of Chemistry.

4.6.1 Boltzman transport equation analysis

In order to analyze the experimental data, Boltzaman transport equation (BTE) approach was used with the relaxation time approximation (RTA). In the framework of this BTE-RTA approach the thermal conductivity can be written as [19, 98]:

$$K_G = \frac{1}{4\pi K_B T^2 h} \sum_{s=LA,TA,ZA} \int_0^{q_{max}} \{[h\omega_s(q)\frac{d\omega_s(q)}{dq}]^2 \tau_{total}(s,q) \frac{exp[h\omega_S(q)/K_B T]}{[exp[h\omega_s(q)/K_B T]-1]^2} q\} dq \tag{4.2}$$

where h = 0.335 nm is the graphene layer thickness, and the summation is performed over all acoustic phonon branches s=LA, TA or ZA, ω_s is the phonon frequency of the s-th phonon branch, q is the phonon wave number, $\tau_{total}(s,q)$ is the total phonon relaxation time, T is the absolute temperature, h and K_B are Plank's and Boltzmann's constant, respectively. The scattering rates for the three main phonon relaxation processes, phonon-phonon Umklapp (U) scattering, phonon-rough-edge scattering (B) and phonon-point-defect (PD) scattering, are given by:

$$\frac{1}{\tau_B(s,q)} = \frac{v_s}{L} \times \frac{(1-p)}{(1+p)} \frac{1}{\tau_{PD}(s,q)} = \frac{S_0 \Gamma q_s \omega_s^2}{4 v_s} \tau_{U,s} = \frac{1}{\gamma_s^2} \times \frac{M v_s^2}{K_B T} \times \frac{\omega_{s,max}}{\omega^2} \tag{4.3}$$

Here $v_s = d\omega_s/dq$ is the phonon group velocity, p is the specularity parameter introduced above, S_0 is the surface per atom, $\omega_{s,max}$ is the maximum cut-off frequency for a given branch, γ_s is an average Gruneisen parameter of the branch s, M is the mass of an unit cell, $\Gamma = \xi(N_d/N_G)$ is the measure of the strength of the point defect scattering and $N_G = 3.8 \times 10^{15} cm^{-2}$ is the concentration of carbon atoms. For analysis of the experimental data, three main mechanisms of phonon scattering were taken into account: phonon phonon Umklapp (U) scattering, phonon rough edge scattering (also referred to as bound-

ary (B) scattering), and phonon point-defect (PD) scattering. Within the relaxation time approximation (RTA), the total relaxation rate is given as:

$$\frac{1}{\tau_{total}(s,q)} = \frac{1}{\tau_U(s,q)} + \frac{1}{\tau_B(s,q)} + \frac{1}{\tau_{PD}(s,q)} \tag{4.4}$$

where the index s=LA, TA, or ZA enumerates longitudinal acoustic (LA), transverse acoustic (TA), and out-of-plane acoustic (ZA) phonon polarization branches, and q is the phonon wave number. The dependence of the thermal conductivity on the defect density, calculated from BTE within the RTA for different values of the specularity parameter p, is presented in Fig. 4.13 by solid curves. The specularity parameter depends on the roughness of the edge and defines the probability of specular scattering of the phonons. For p=1, the scattering of phonons is purely specular, which means that the edge scattering does not introduce extra thermal resistance. For p=0, the scattering is fully diffuse, which corresponds to the strongest thermal resistance from the graphene edges [11, 19]. The experimentally observed trend in thermal conductivity can be recovered with the reasonable values of the specularity parameter changing from p=0.5 to p=0.9 [19].

The strength of the phonon scattering on defects is determined by the mass-difference parameter $\xi = (\Delta M/M)^2$, where M is the mass of carbon atom and $\Delta M = M - M_D$ is the difference between masses of a carbon atom and a defect. The value of ξ strongly depends on the nature of defects. In this BTE analysis, ξ was used as a fitting parameter to the experimental data. Within this model assumptions, the agreement with the experimental results is reached for ξ= 590. The perturbation theory calculations [99] for pure vacancy defects in graphite estimate the value of the parameter to be $\xi \sim 9$. This is substantially smaller than the fitting value to the experimental data. The latter is explained by the fact

that the model used here assumes only one type of phonon-defect scattering: mass-difference scattering on single vacancies. In reality, the samples under this study contain a variety of defects, including those that were present before irradiation and those induced by irradiation, which are different from simple vacancies. Thus, large ξ imitates the effect of phonon scattering on all other types of defects. The expected defect clustering will also result in higher ξ than that calculated from the perturbation theory under point-defect assumption. The important conclusion from the BTE modeling is that the observed weakening $K(N_D)$ dependence can be reproduced via interplay of the three main phonon scattering mechanisms-mklapp scattering due to lattice anharmonicity, mass-difference scattering, and rough edge scattering.

4.6.2 Molecular dynamics (MD) simulation

In this section the possible nature of defects in the samples and their effect on the thermal conductivity will be studied as revealed from MD simulations. Simulations are performed on a pristine graphene sheet of size 319.5 nm 54.1 nm containing 660,000 carbon (C) atoms. Defects (single and double vacancies) are introduced in the structure by randomly selecting and removing carbon atoms. The $C - C$ interactions are described using the optimized Tersoff potential for thermal transport in graphene [100]. Periodic boundary conditions are employed in all directions. The simulations are carried out with the LAMMPS package [68]. The graphene structure is energy minimized and subsequently simulated under the isothermal-isobaric (NPT) ensemble using the Nose-Hoover thermostat at 300 K and barostat at 0 MPa for 4 ns, followed by equilibration in canonical (NVT) ensemble for 4 ns using the Nose-Hoover thermostat at 300 K. The coupling time for thermostats are 0.1

ps and that for barostat is 1 ps. The thermodynamic constraints are removed and the structure is simulated under the microcanonical (NVE) ensemble for 3 ns to ensure equilibration. Subsequently, thermal conductivity is computed using the reverse non-equilibrium MD technique [101, 102]. The time step of integration used in all the simulations is 1 fs.

The electron energies of 20 keV used in the electron beam irradiation process are less than the knockout threshold energy of 80 keV [86, 103–105]. Such irradiation is only sufficient to overcome the energy barrier required for breaking of the carbon-carbon bond and initiating reaction with any residual impurities such as H_2O and O_2 on the surface of graphene. This reaction results in functionalization of graphene with $-OH$ and $-C=O$ groups. Prior studies have shown that the $C=O$ configuration is energetically more favorable than OH, and the transition of OH and other functional groups into the energetically stable $C=O$ configuration can occur especially when they are annealed [106]. The energy barrier for the diffusion of $-OH$ and epoxy groups is around 0.5-0.7 eV [107], which corresponds to a diffusion rate $\sim 102\ s^{-1}$ as calculated from transition-state theory, assuming a typical phonon frequency range in graphene. For this reason, the functional groups can be mobile at the temperature of the thermal experiments (350 K). Upon continuous electron beam irradiation, two epoxy or hydroxyl group can come together and release an O_2 molecule [107]. When the coverage of functional groups is high, detectable amounts of CO/CO_2 can be released creating vacancies in the graphene lattice [108]. The presence of $-OH$ and $-C=O$ functional groups can be the reason for stronger phonon-defect scattering than that predicted by BTE models with vacancies only (and the resulting large ξ required for fitting to the experimental data). The MD simulations show that a combination of

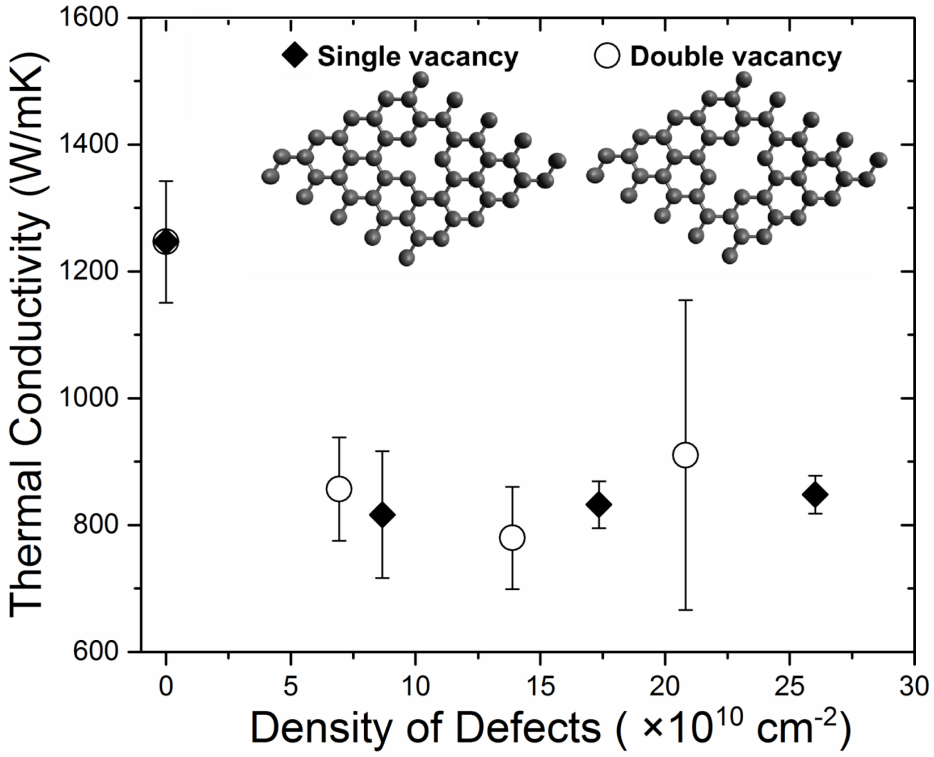

Figure 4.14: Molecular dynamics simulation results for thermal conductivity of graphene with single and double vacancy defects. The simulated defect structures are depicted in the inset. The results show that the contributions of single and double vacancies are similar in reducing the thermal conductivity of graphene. The results are in line with the experimental trend. The absolute value at the zero-defect limit is lower than the experimental due to the domain-size limitation in the simulation. The figure is reproduced from H. Malekpour, P. Ramnani, S. Srinivasan, G. Balasubramanian, D. L. Nika, A. Mulchandani, R. K. Lake, A. A. Balandin, *Nanoscale* **8**, 14608 (2016) with permission from Royal Society of Chemistry.

single and double vacancy defects can also account for the experimentally observed thermal conductivity dependence on the defect concentration. The absolute value at the zero-defect limit is lower than the experimental due to the domain-size limitation in the simulation.

Fig. 4.14 shows that thermal conductivity decreases drastically as N_D increases from $2 \times 10^{10} cm^{-2}$ to $10 \times 10^{10} cm^{-2}$ and reaches a near-constant value at the higher concentrations of defects. This value is substantially above the amorphous carbon limit, in line with the experiment. According to this model scenario, upon irradiation, $-C = O$ and other functionalized defects are formed that strongly reduce the thermal conductivity. Continuous irradiation results in the creation of single and double vacancies. The increase in their concentration does not lead to pronounced K reduction, which approaches an approximately constant value for the N_D range that was investigated. It can be explained in the following way. As more defects are introduced in graphene through irradiation the additional defect sites serve as scattering centers for phonons with wavelengths shorter than the distance between two vacancies. The delocalized long-wavelength phonons, that carry a significant fraction of heat, are less affected by extra defects that are closely spaced compared to those introduced at the previous irradiation step. At some irradiation dose, the increase in the phonon scattering rate of the delocalized modes due to extra defects is substantially smaller than that of the short-ranged localized modes. Hence, after a certain critical N_D the thermal conductivity effectively saturates. The weakening of the $K(N_D)$ dependence observed experimentally and reveled in the present MD simulation is in line with reported computational results performed for graphene and graphene ribbons [109–112].

Chapter 5

Conclusions

In this dissertation I've studied thermal properties of different graphene-derivatives using OTR technique: Graphene laminate, reduced graphene oxide film and graphene with ebeam induced defects. In the fisrt part of the dissertation thermal conductivity of graphene laminate film deposited on PET substrate was in order to investigate the possibility of making plastic thermally conductive. PET is widely used in packaging industery and a conductive PET can be beneficial in many applications such as packaging industery where dissipating excess heat is needed. Two different types of laminates were studied: as-deposited and compressed. It was found that thermal conductivity of graphene laminate films on PET varies from 40 to 90 W/mK at RT. Graphene laminate is made of overlapping single layer and multi layer graphene flakes. After a detailed statistical analysis on the average flake size it was found that the average size and the alignment of graphene flakes are more important parameters defining the heat conduction than the mass density of the graphene laminate. The thermal conductivity scales up linearly with the average graphene flake size in both

as deposited and compressed laminates. The compressed laminates have higher thermal conductivity for the same average flake size owing to better flake alignment. The possibility of coating plastic materials with thin graphene laminates that have more than two orders-of-magnitude higher thermal conductivity can be used for improving thermal management of electronic and optoelectronic packaging.

One of the interesting facts about this study was that the high thermal conductivity values of GL were achieved in both uncompressed and compressed GL-on-PET. This suggests that for practical applications, graphene coating can be beneficial for improving heat conduction properties of plastics without roll compression or any other processing steps. The plastic material used in this study, polyethylene terephthalate, is widely used in packaging industry such as water bottles or soft drink. The low cost, durability and lightweight of plastics makes it beneficial for packaging industry. However in many cases, the insulating behavior of plastic is not desirable and limits many possible applications. New applications of plastic materials, e.g. packaging or housing of electronic components, require higher values of thermal conductivity. This is mainly due to the increasing dissipated heat densities for modern electronics and optoelectronics. The described thermal data suggests that graphene laminates could be applied as potential thermal coatings in such applications. It has been demonstrated that graphene laminate coatings could improve the thermal conductivity of plastic materials up to 600 times. Thus, a significant increase in the potential range of practical applications of plastics could be achieved, allowing them to be used in areas not feasible till now. This study could be a significant progress for improving thermal management of electronic and optoelectronic packaging.

Considering the significance of graphene and few layer graphene in thermal management applications such as thermal interface materials, thermal coatings and pads, there is a demand to develop methods to scale up the production of graphene sheets. The reduction of grapehne oxide has been attracted lots of attention for this purpose. The possibility of using an inexpensive natural graphite as the raw material along with the excellent properties of graphite oxide to easily exfoliate in water solution, makes the reduction technique a promising industry-compatible technique for production of grahene sheets. However, the quality of graphene produced by this technbique is lower compared to the theoretical potential of pristine graphene and compared to other methods such as mechanical exfoliation. This cost effective lower quality graphene can still be useful for applications, such as thermal management, where exploiting high intrinsic electrical and thermal properties of graphene is not critical. In the second part of this dissertation, thermal conductivity of freestanding chemically reduced graphene oxide films were studied. The layered structure of the films makes them strongly anisotropic in thermal conduction and therefore a combination of two different techniques were used to extract both the in-plane and cross-plane thermal conductivity values. The two methods include the transient laser flash and the steady state Raman opto-thermal techniques. The in-plane thermal conductivity values of 11-45 W/mK have been achieved for the chemically reduced graphene oxide films which shows up to 15 times increase in thermal conductivity compared to graphene oxide film. It was found that the in-plane thermal conductivity increases with increasing carbon concentration. Electrical conductivity exhibits similar behavior. This could be explained by the formation of more sp^2 phases, confirmed by the Raman studies. The theoretical calculation suggests that the

average graphitic cluster size might affect this increasing trend. On the other hands, the cross-plane thermal conductivity values show a direct correlation to the film microstructure and morphology. Low cross-plane thermal conductivity values ~ 0.1 to ~ 1.0 $W/m.K$ were measured, owing to the layered structure of the films. The study is important for the use of rGO in thermal management applications.

Graphene [32] has exceptionally high intrinsic thermal conductivity, ~ 4000 – 6000 W/mK [7, 10]. However, this high value of thermal conductivity can be degraded by defects such as polymer residue from nanofabrication [73], edge roughness [19], polycrystalline grain boundaries [74], and disorder from contact with a substrate or a capping layer [25, 75, 76]. For this reason, the thermal conductivity of graphene synthesized by the chemical vapor deposition (CVD) is always lower than that of the mechanically exfoliated graphene from highly ordered pyrolytic graphite (HOPG) [7, 24, 34–36]. A possible loss of polycrystalline grain orientation in the average quality CVD graphene can lead to additional degradation of the thermal conductivity [77]. However, to date, there have been no quantitative experimental studies of the thermal conductivity dependence on the concentration of defects, N_D, in graphene. The knowledge of the K dependence on the concentration of defects induced by irradiation can shed light on the strength of the phonon-point defect scattering in 2-D materials. The change in the dimensionality results in different dependencies of the scattering rates on the phonon wavelengths in the processes of phonon relaxation by defects and grain boundaries [13, 19, 67]. In the third part of this dissertation, thermal conductivity of suspended CVD graphene was studied as a function of the defect density. The defects were introduced by the low-energy electron beams and quantified by the Raman D-to-G peak in-

tensity ratios. It was found that as the defect density changes from $2.0{\times}10^{10}$ cm^2 to $1.8{\times}10^{11}$ cm^2 the thermal conductivity reduces from $\sim (1.8 \pm 0.2) \times 10^3$ W/mK to $\sim (4.0 \pm 0.2) \times 10^2$ W/mK near RT. At higher defect density the thermal conductivity revealed an intriguing weakening of the $K(N_D)$ dependence. This behavior was explained theoretically within the Boltzmann transport equation and molecular dynamics approaches. The obtained results contribute to understanding the acoustic phonon-point defect scattering in 2D materials. My data indicating rather large values of thermal conductivity for graphene with defects adds validity to the proposed practical applications of graphene in thermal management.

Bibliography

[1] H Malekpour et al. "Thermal conductivity of graphene laminate". In: *Nano letters* 14.9 (2014), pp. 5155–5161.

[2] Hoda Malekpour et al. "Thermal conductivity of graphene with defects induced by electron beam irradiation". In: *Nanoscale* 8.30 (2016), pp. 14608–14616.

[3] Alexander Balandin. "Thermal properties of semiconductor low-dimensional structures". In: *Phys. Low-Dimens. Struct* 1.2 (2000), pp. 1–2.

[4] PG Klemens. "Solid state physics". In: *Academic, New York* (1958), p. 7.

[5] John Edwin Parrott and Audrey D Stuckes. "Thermal conductivity of solids". In: (1975).

[6] HJ Goldsmid. "The thermal conductivity of bismuth telluride". In: *Proceedings of the Physical Society. Section B* 69.2 (1956), p. 203.

[7] Alexander A Balandin et al. "Superior thermal conductivity of single-layer graphene". In: *Nano letters* 8.3 (2008), pp. 902–907.

[8] Zhenhua Ni et al. "Raman spectroscopy and imaging of graphene". In: *Nano Research* 1.4 (2008), pp. 273–291.

[9] Konstantin S Novoselov et al. "A roadmap for graphene". In: *Nature* 490.7419 (2012), pp. 192–200.

[10] Alexander A Balandin. "Thermal properties of graphene and nanostructured carbon materials". In: *Nature materials* 10.8 (2011), pp. 569–581.

[11] Denis L Nika, Artur S Askerov, and Alexander A Balandin. "Anomalous size dependence of the thermal conductivity of graphene ribbons". In: *Nano letters* 12.6 (2012), pp. 3238–3244.

[12] Denis L Nika, Evghenii P Pokatilov, and Alexander A Balandin. "Theoretical description of thermal transport in graphene: The issues of phonon cut-off frequencies and polarization branches". In: *physica status solidi (b)* 248.11 (2011), pp. 2609–2614.

[13] PG Klemens. "Theory of the a-plane thermal conductivity of graphite". In: *Journal of Wide Bandgap Materials* 7.4 (2000), pp. 332–339.

[14] Denis L Nika and Alexander A Balandin. "Two-dimensional phonon transport in graphene". In: *Journal of Physics: Condensed Matter* 24.23 (2012), p. 233203.

[15] PG Klemens. "Phonon scattering and thermal resistance due to grain boundaries". In: *International journal of thermophysics* 15.6 (1994), pp. 1345–1351.

[16] Subhash L Shindé and Jitendra Goela. *High thermal conductivity materials*. Vol. 91. Springer, 2006.

[17] Philippe Gonnet et al. "Thermal conductivity of magnetically aligned carbon nanotube buckypapers and nanocomposites". In: *Current Applied Physics* 6.1 (2006), pp. 119–122.

[18] Zhidong Han and Alberto Fina. "Thermal conductivity of carbon nanotubes and their polymer nanocomposites: a review". In: *Progress in polymer science* 36.7 (2011), pp. 914–944.

[19] DL Nika et al. "Phonon thermal conduction in graphene: Role of Umklapp and edge roughness scattering". In: *Physical Review B* 79.15 (2009), p. 155413.

[20] L Lindsay, DA Broido, and Natalio Mingo. "Diameter dependence of carbon nanotube thermal conductivity and extension to the graphene limit". In: *Physical Review B* 82.16 (2010), p. 161402.

[21] S Mei et al. "Full-dispersion Monte Carlo simulation of phonon transport in micron-sized graphene nanoribbons". In: *Journal of Applied Physics* 116.16 (2014), p. 164307.

[22] Giorgia Fugallo et al. "Thermal conductivity of graphene and graphite: collective excitations and mean free paths". In: *Nano letters* 14.11 (2014), pp. 6109–6114.

[23] Suchismita Ghosh et al. "Dimensional crossover of thermal transport in few-layer graphene". In: *Nature materials* 9.7 (2010), pp. 555–558.

[24] Weiwei Cai et al. "Thermal transport in suspended and supported monolayer graphene grown by chemical vapor deposition". In: *Nano letters* 10.5 (2010), pp. 1645–1651.

[25] Jae Hun Seol et al. "Two-dimensional phonon transport in supported graphene". In: *Science* 328.5975 (2010), pp. 213–216.

[26] Khan MF Shahil and Alexander A Balandin. "Graphene–multilayer graphene nanocomposites as highly efficient thermal interface materials". In: *Nano letters* 12.2 (2012), pp. 861–867.

[27] Jackie D Renteria, Denis L Nika, and Alexander A Balandin. "Graphene thermal properties: applications in thermal management and energy storage". In: *Applied Sciences* 4.4 (2014), pp. 525–547.

[28] Zhong Yan, Denis L Nika, and Alexander A Balandin. “Thermal properties of graphene and few-layer graphene: applications in electronics”. In: *IET Circuits, Devices & Systems* 9.1 (2015), pp. 4–12.

[29] Zhong Yan et al. “Graphene quilts for thermal management of high-power GaN transistors”. In: *Nature communications* 3 (2012), p. 827.

[30] Sang-Hoon Bae et al. “Graphene-based heat spreader for flexible electronic devices”. In: *IEEE Transactions on Electron Devices* 61.12 (2014), pp. 4171–4175.

[31] Pradyumna Goli et al. “Thermal properties of graphene–copper–graphene heterogeneous films”. In: *Nano letters* 14.3 (2014), pp. 1497–1503.

[32] Andre K Geim and Konstantin S Novoselov. “The rise of graphene”. In: *Nature materials* 6.3 (2007), pp. 183–191.

[33] Jackie D Renteria et al. “Strongly Anisotropic Thermal Conductivity of Free-Standing Reduced Graphene Oxide Films Annealed at High Temperature”. In: *Advanced Functional Materials* 25.29 (2015), pp. 4664–4672.

[34] Luis A Jauregui et al. “Thermal transport in graphene nanostructures: Experiments and simulations”. In: *Ecs Transactions* 28.5 (2010), pp. 73–83.

[35] S Ghosh et al. “Extremely high thermal conductivity of graphene: Prospects for thermal management applications in nanoelectronic circuits”. In: *Applied Physics Letters* 92.15 (2008), p. 151911.

[36] Hongyang Li et al. “Thermal conductivity of twisted bilayer graphene”. In: *Nanoscale* 6.22 (2014), pp. 13402–13408.

[37] Graeme Williams, Brian Seger, and Prashant V Kamat. “TiO2-graphene nanocomposites. UV-assisted photocatalytic reduction of graphene oxide”. In: *ACS nano* 2.7 (2008), pp. 1487–1491.

[38] William S Hummers Jr and Richard E Offeman. “Preparation of graphitic oxide”. In: *Journal of the American Chemical Society* 80.6 (1958), pp. 1339–1339.

[39] Cristina Gómez-Navarro et al. “Electronic transport properties of individual chemically reduced graphene oxide sheets”. In: *Nano letters* 7.11 (2007), pp. 3499–3503.

[40] Songfeng Pei and Hui-Ming Cheng. “The reduction of graphene oxide”. In: *Carbon* 50.9 (2012), pp. 3210–3228.

[41] Tamás Szabó et al. “Evolution of surface functional groups in a series of progressively oxidized graphite oxides”. In: *Chemistry of materials* 18.11 (2006), pp. 2740–2749.

[42] C Hontoria-Lucas et al. “Study of oxygen-containing groups in a series of graphite oxides: physical and chemical characterization”. In: *Carbon* 33.11 (1995), pp. 1585–1592.

[43] Hae-Kyung Jeong et al. “Evidence of graphitic AB stacking order of graphite oxides”. In: *Journal of the American Chemical Society* 130.4 (2008), pp. 1362–1366.

[44] Hannes C Schniepp et al. “Functionalized single graphene sheets derived from splitting graphite oxide”. In: *The Journal of Physical Chemistry B* 110.17 (2006), pp. 8535–8539.

[45] Cecilia Mattevi et al. “Evolution of electrical, chemical, and structural properties of transparent and conducting chemically derived graphene thin films”. In: *Advanced Functional Materials* 19.16 (2009), pp. 2577–2583.

[46] Kyoung Hwan Kim et al. “High quality reduced graphene oxide through repairing with multi-layered graphene ball nanostructures”. In: *Scientific reports* 3 (2013).

[47] C-H Chuang et al. “The effect of thermal reduction on the photoluminescence and electronic structures of graphene oxides”. In: *Scientific reports* 4 (2014), p. 4525.

[48] Mohamed Boutchich et al. “Characterization of graphene oxide reduced through chemical and biological processes”. In: *Journal of Physics: Conference Series*. Vol. 433. 1. IOP Publishing. 2013, p. 012001.

[49] Mukesh Singh et al. “Annealing induced electrical conduction and band gap variation in thermally reduced graphene oxide films with different sp 2/sp 3 fraction”. In: *Applied Surface Science* 326 (2015), pp. 236–242.

[50] Xavier Díez-Betriu et al. “Raman spectroscopy for the study of reduction mechanisms and optimization of conductivity in graphene oxide thin films”. In: *Journal of Materials Chemistry C* 1.41 (2013), pp. 6905–6912.

[51] Vicente López et al. “Chemical vapor deposition repair of graphene oxide: a route to highly-conductive graphene monolayers”. In: *Advanced Materials* 21.46 (2009), p. 4683.

[52] Songfeng Pei et al. “Direct reduction of graphene oxide films into highly conductive and flexible graphene films by hydrohalic acids”. In: *Carbon* 48.15 (2010), pp. 4466–4474.

[53] Héctor A Becerril et al. “Evaluation of solution-processed reduced graphene oxide films as transparent conductors”. In: *ACS nano* 2.3 (2008), pp. 463–470.

[54] Zhongqing Wei et al. “Nanoscale tunable reduction of graphene oxide for graphene electronics”. In: *Science* 328.5984 (2010), pp. 1373–1376.

[55] Tengfei Qiu et al. “Hydrogen reduced graphene oxide/metal grid hybrid film: towards high performance transparent conductive electrode for flexible electrochromic devices”. In: *Carbon* 81 (2015), pp. 232–238.

[56] Yong Zhou et al. “Microstructuring of graphene oxide nanosheets using direct laser writing”. In: *Advanced Materials* 22.1 (2010), pp. 67–71.

[57] Dongxing Yang et al. “Chemical analysis of graphene oxide films after heat and chemical treatments by X-ray photoelectron and Micro-Raman spectroscopy”. In: *Carbon* 47.1 (2009), pp. 145–152.

[58] Tran Viet Cuong et al. “Photoluminescence and Raman studies of graphene thin films prepared by reduction of graphene oxide”. In: *Materials letters* 64.3 (2010), pp. 399–401.

[59] Hailiang Wang et al. “Solvothermal reduction of chemically exfoliated graphene sheets”. In: *Journal of the American Chemical Society* 131.29 (2009), pp. 9910–9911.

[60] L Gustavo Cançado et al. “Quantifying defects in graphene via Raman spectroscopy at different excitation energies”. In: *Nano letters* 11.8 (2011), pp. 3190–3196.

[61] Andrea C Ferrari and Jf Robertson. “Interpretation of Raman spectra of disordered and amorphous carbon”. In: *Physical review B* 61.20 (2000), p. 14095.

[62] F Tuinstra and J L_ Koenig. “Raman spectrum of graphite”. In: *The Journal of Chemical Physics* 53.3 (1970), pp. 1126–1130.

[63] I Calizo et al. “Temperature dependence of the Raman spectra of graphene and graphene multilayers”. In: *Nano letters* 7.9 (2007), pp. 2645–2649.

[64] EH Martins Ferreira et al. “Evolution of the Raman spectra from single-, few-, and many-layer graphene with increasing disorder”. In: *Physical Review B* 82.12 (2010), p. 125429.

[65] Alexandr I Cocemasov, Denis L Nika, and Alexander A Balandin. “Phonons in twisted bilayer graphene”. In: *Physical Review B* 88.3 (2013), p. 035428.

[66] Denis L Nika, Alexandr I Cocemasov, and Alexander A Balandin. “Specific heat of twisted bilayer graphene: Engineering phonons by atomic plane rotations”. In: *Applied Physics Letters* 105.3 (2014), p. 031904.

[67] PG Klemens and DF Pedraza. “Thermal conductivity of graphite in the basal plane”. In: *Carbon* 32.4 (1994), pp. 735–741.

[68] DL Nika et al. “Lattice thermal conductivity of graphene flakes: Comparison with bulk graphite”. In: *Applied Physics Letters* 94.20 (2009), p. 203103.

[69] Z Aksamija and I Knezevic. “Lattice thermal conductivity of graphene nanoribbons: Anisotropy and edge roughness scattering”. In: *Applied Physics Letters* 98.14 (2011), p. 141919.

[70] Shanshan Chen et al. “Raman measurements of thermal transport in suspended monolayer graphene of variable sizes in vacuum and gaseous environments”. In: *ACS nano* 5.1 (2010), pp. 321–328.

[71] Kichul Yoon et al. “Measuring the thermal conductivity of residue-free suspended graphene bridge using null point scanning thermal microscopy”. In: *Carbon* 76 (2014), pp. 77–83.

[72] Stefano Lepri, Roberto Livi, and Antonio Politi. “Thermal conduction in classical low-dimensional lattices”. In: *Physics reports* 377.1 (2003), pp. 1–80.

[73] Michael Thompson Pettes et al. “Influence of polymeric residue on the thermal conductivity of suspended bilayer graphene”. In: *Nano letters* 11.3 (2011), pp. 1195–1200.

[74] Andrey Y Serov, Zhun-Yong Ong, and Eric Pop. “Effect of grain boundaries on thermal transport in graphene”. In: *Applied Physics Letters* 102.3 (2013), p. 033104.

[75] Keiji Saito and Abhishek Dhar. “Heat conduction in a three dimensional anharmonic crystal”. In: *Physical review letters* 104.4 (2010), p. 040601.

[76] Zhun-Yong Ong and Eric Pop. “Effect of substrate modes on thermal transport in supported graphene”. In: *Physical Review B* 84.7 (2011), p. 075471.

[77] Z Aksamija and I Knezevic. “Lattice thermal transport in large-area polycrystalline graphene”. In: *Physical Review B* 90.3 (2014), p. 035419.

[78] Shanshan Chen et al. “Thermal conductivity of isotopically modified graphene”. In: *Nature materials* 11.3 (2012), pp. 203–207.

[79] B Abeles. “Lattice thermal conductivity of disordered semiconductor alloys at high temperatures”. In: *Physical Review* 131.5 (1963), p. 1906.

[80] Weili Liu and Alexander A Balandin. “Thermal conduction in AlxGa1-xN alloys and thin films”. In: *Journal of Applied Physics* 97.7 (2005), pp. 73710–73710.

[81] Samia Subrina, Dmitri Kotchetkov, and Alexander A Balandin. “Heat removal in silicon-on-insulator integrated circuits with graphene lateral heat spreaders”. In: *IEEE Electron Device Letters* 30.12 (2009), pp. 1281–1283.

[82] Zhaoli Gao et al. “Thermal chemical vapor deposition grown graphene heat spreader for thermal management of hot spots”. In: *Carbon* 61 (2013), pp. 342–348.

[83] Vivek Goyal and Alexander A Balandin. “Thermal properties of the hybrid graphene-metal nano-micro-composites: Applications in thermal interface materials”. In: *Applied Physics Letters* 100.7 (2012), p. 073113.

[84] Khan MF Shahil and Alexander A Balandin. “Thermal properties of graphene and multilayer graphene: Applications in thermal interface materials”. In: *Solid State Communications* 152.15 (2012), pp. 1331–1340.

[85] Qingkai Yu et al. “Control and characterization of individual grains and grain boundaries in graphene grown by chemical vapour deposition”. In: *Nature materials* 10.6 (2011), pp. 443–449.

[86] Desalegne Teweldebrhan and Alexander A Balandin. “Modification of graphene properties due to electron-beam irradiation”. In: *Applied Physics Letters* 94.1 (2009), p. 013101.

[87] Guanxiong Liu, Desalegne Teweldebrhan, and Alexander A Balandin. “Tuning of graphene properties via controlled exposure to electron beams”. In: *IEEE Transactions on Nanotechnology* 10.4 (2011), pp. 865–870.

[88] Cho Yen Ho, Reginald W Powell, and PE Liley. “Thermal conductivity of the elements”. In: *Journal of Physical and Chemical Reference Data* 1.2 (1972), pp. 279–421.

[89] Márcia Maria Lucchese et al. “Quantifying ion-induced defects and Raman relaxation length in graphene”. In: *Carbon* 48.5 (2010), pp. 1592–1597.

[90] Pedro Venezuela, Michele Lazzeri, and Francesco Mauri. “Theory of double-resonant Raman spectra in graphene: intensity and line shape of defect-induced and two-phonon bands”. In: *Physical Review B* 84.3 (2011), p. 035433.

[91] Axel Eckmann et al. “Probing the nature of defects in graphene by Raman spectroscopy”. In: *Nano letters* 12.8 (2012), pp. 3925–3930.

[92] LG Cancado et al. “Influence of the atomic structure on the Raman spectra of graphite edges”. In: *Physical review letters* 93.24 (2004), p. 247401.

[93] Cinzia Casiraghi et al. “Raman spectroscopy of graphene edges”. In: *Nano letters* 9.4 (2009), pp. 1433–1441.

[94] Benjamin Krauss et al. “Raman scattering at pure graphene zigzag edges”. In: *Nano letters* 10.11 (2010), pp. 4544–4548.

[95] Kin Fai Mak et al. “Measurement of the optical conductivity of graphene”. In: *Physical review letters* 101.19 (2008), p. 196405.

[96] Iman Santoso et al. “Tunable optical absorption and interactions in graphene via oxygen plasma”. In: *Physical Review B* 89.7 (2014), p. 075134.

[97] Guang-Xin Ni et al. “Tuning Optical Conductivity of Large-Scale CVD Graphene by Strain Engineering”. In: *Advanced Materials* 26.7 (2014), pp. 1081–1086.

[98] Ajit K Vallabhaneni et al. “Reliability of Raman measurements of thermal conductivity of single-layer graphene due to selective electron-phonon coupling: A first-principles study”. In: *Physical Review B* 93.12 (2016), p. 125432.

[99] CA Ratsifaritana and PG Klemens. "Scattering of phonons by vacancies". In: *International journal of thermophysics* 8.6 (1987), pp. 737–750.

[100] Helin Cao et al. "Electronic transport in chemical vapor deposited graphene synthesized on Cu: Quantum Hall effect and weak localization". In: *arXiv preprint arXiv:0910.4329* (2009).

[101] L Lindsay and DA Broido. "Optimized Tersoff and Brenner empirical potential parameters for lattice dynamics and phonon thermal transport in carbon nanotubes and graphene". In: *Physical Review B* 81.20 (2010), p. 205441.

[102] Steve Plimpton. "Fast parallel algorithms for short-range molecular dynamics". In: *Journal of computational physics* 117.1 (1995), pp. 1–19.

[103] J Kotakoski et al. "From point defects in graphene to two-dimensional amorphous carbon". In: *Physical Review Letters* 106.10 (2011), p. 105505.

[104] Florian Banhart, Jani Kotakoski, and Arkady V Krasheninnikov. "Structural defects in graphene". In: *ACS nano* 5.1 (2010), pp. 26–41.

[105] Tianli Feng et al. "Spectral phonon mean free path and thermal conductivity accumulation in defected graphene: The effects of defect type and concentration". In: *Physical Review B* 91.22 (2015), p. 224301.

[106] Akbar Bagri et al. "Stability and formation mechanisms of carbonyl-and hydroxyl-decorated holes in graphene oxide". In: *The Journal of Physical Chemistry C* 114.28 (2010), pp. 12053–12061.

[107] Si Zhou and Angelo Bongiorno. "Origin of the chemical and kinetic stability of graphene oxide". In: *Scientific reports* 3 (2013).

[108] Rosanna Larciprete et al. "Dual path mechanism in the thermal reduction of graphene oxide". In: *Journal of the American Chemical Society* 133.43 (2011), pp. 17315–17321.

[109] Hengji Zhang, Geunsik Lee, and Kyeongjae Cho. "Thermal transport in graphene and effects of vacancy defects". In: *Physical Review B* 84.11 (2011), p. 115460.

[110] Feng Hao, Daining Fang, and Zhiping Xu. "Mechanical and thermal transport properties of graphene with defects". In: *Applied physics letters* 99.4 (2011), p. 041901.

[111] Bohayra Mortazavi and Saïd Ahzi. "Thermal conductivity and tensile response of defective graphene: a molecular dynamics study". In: *Carbon* 63 (2013), pp. 460–470.

[112] Justin Haskins et al. "Control of thermal and electronic transport in defect-engineered graphene nanoribbons". In: *ACS nano* 5.5 (2011), pp. 3779–3787.

[113] S Ghosh et al. "Heat conduction in graphene: experimental study and theoretical interpretation". In: *New Journal of Physics* 11.9 (2009), p. 095012.

[114] Vincent E Dorgan et al. “High-field electrical and thermal transport in suspended graphene”. In: *Nano letters* 13.10 (2013), pp. 4581–4586.

[115] Raghunath Murali et al. “Breakdown current density of graphene nanoribbons”. In: *Applied Physics Letters* 94.24 (2009), p. 243114.

[116] Rusen Yan et al. “Thermal conductivity of monolayer molybdenum disulfide obtained from temperature-dependent Raman spectroscopy”. In: *ACS nano* 8.1 (2014), pp. 986–993.

[117] Z Yan et al. “Phonon and thermal properties of exfoliated TaSe2 thin films”. In: *Journal of Applied Physics* 114.20 (2013), p. 204301.

[118] Florian Müller-Plathe. “A simple nonequilibrium molecular dynamics method for calculating the thermal conductivity”. In: *The Journal of chemical physics* 106.14 (1997), pp. 6082–6085.

[119] Ganesh Balasubramanian et al. “Thermal conductivity reduction through isotope substitution in nanomaterials: predictions from an analytical classical model and nonequilibrium molecular dynamics simulations”. In: *Nanoscale* 3.9 (2011), pp. 3714–3720.